NUMERICAL AND EXPERIMENTAL STUDIES OF DAMAGE GENERATION IN MULTI-LAYER COMPOSITE MATERIALS AT HIGH STRAIN RATES

submitted by

I. W. Hall
Department of Mechanical Engineering
University of Delaware
Newark, DE 19716

Foreword

This report concerns the results of a S.T.I.R. Program carried out between March and November 2005. The general objectives of the program were to demonstrate the feasibility and utility of a novel use of the Split Hopkinson Pressure Bar (SHPB) as a tool for the investigation and development of multi-layered materials for high strain rate applications.

Report Documentation Page

Form Approved
OMB No. 0704-0188

1. REPORT DATE	2. REPORT TYPE	3. DATES COVERED
05 JAN 2006	**N/A**	**-**

4. TITLE AND SUBTITLE	5a. CONTRACT NUMBER
Numerical and Experimental Studies of Damage Generation in Multi-Layer Composite Materials at High Strain Rates	5b. GRANT NUMBER
	5c. PROGRAM ELEMENT NUMBER
6. AUTHOR(S)	5d. PROJECT NUMBER
	5e. TASK NUMBER
	5f. WORK UNIT NUMBER
7. PERFORMING ORGANIZATION NAME(S) AND ADDRESS(ES) **U.S. Army Research Office P.O. Box 12211 Research Triangle Park, NC 27709-2211**	8. PERFORMING ORGANIZATION REPORT NUMBER
9. SPONSORING/MONITORING AGENCY NAME(S) AND ADDRESS(ES)	10. SPONSOR/MONITOR'S ACRONYM(S)
	11. SPONSOR/MONITOR'S REPORT NUMBER(S)

12. DISTRIBUTION/AVAILABILITY STATEMENT
Approved for public release, distribution unlimited

13. SUPPLEMENTARY NOTES
The original document contains color images.

14. ABSTRACT

15. SUBJECT TERMS

16. SECURITY CLASSIFICATION OF:			17. LIMITATION OF ABSTRACT	18. NUMBER OF PAGES	19a. NAME OF RESPONSIBLE PERSON
a. REPORT	b. ABSTRACT	c. THIS PAGE			
unclassified	**unclassified**	**unclassified**	**UU**	**49**	

Table of Contents

1. **Background**

This report concerns the results of a S.T.I.R. Program carried out between March and November 2005. The general objectives of the program were to demonstrate the feasibility and utility of a novel use of the Split Hopkinson Pressure Bar (SHPB) as a tool for the investigation and development of multi-layered materials for high strain rate applications. Here, the SHPB is *not* used as a device for generating mechanical property data but is, instead, used as a *probe* to generate input and output signals which are then used to validate numerical models.

The principle of the method is to perform an experiment on the SHPB and collect the usual data which accurately define the input wave and the exit waves. Strain gages on the sample itself can provide extra data at specific locations on the sample surface. The numerical model is then developed, based on properties from tests conducted on simple single layer samples. The model comprises the incident and transmitter bars of the SHPB set-up plus the sample: the known incident wave is the model input. Then, when the numerically calculated exit waves exactly match the experimentally determined exit waves the model must be accurately capturing the details of wave propagation, transmission and reflection within the sample itself. This provides the basic validation of the model. Further validation is provided by

a) comparing data calculated for specific locations on the sample with data generated by actual strain gages at the same locations,

b) fractographic and metallographic examination of the samples to verify that the predicted deformation and fracture modes do in fact occur, and

c) high speed photography of actual tests to correlate real events with calculated events.

Early application of this approach has been documented [1] [2] for single and multi-layer materials under essentially elastic deformation conditions. The reader is referred to these articles for more details than are presented here concerning the earlier work that describes the progression from single, through double and finally to triple layered materials.

The specific declared objectives of the research performed under this S.T.I.R Program were to:

a) incorporate plasticity and hyper-elastic deformation into the essentially elastic models already developed and,

b) incorporate damage and failure mechanisms into the models.

2. Introduction

The present research began, then, with relatively simple models capable of describing purely elastic behavior and has progressed to ever more complex cases, with the ultimate goal of incorporating damage and failure effects that may occur in practical materials at realistic strains and strain rates. Consequently, this research has addressed the task of developing tools to investigate the damage evolution-propagation inside multi-layer specimens by a combination of experimental and numerical techniques. FEA modeling of the damage evolution-propagation in multi-layer composite materials necessitates the investigation of the behavior of each individual component first, and then the damage mechanisms are studied in multi-layer materials containing a ceramic front layer and composite backing layers subjected to large strains under high strain rate loading.

The JH-2 and MSC 162 material models were used to simulate the damage evolution and dynamic failure of the ceramic and composite layers respectively. The feasibility of extending the current elastic numerical models for high strain rate loading of complex multi-layer materials into the higher strain and strain rate regimes where significant damage begins to occur has been demonstrated. Critical to the success of this study has been the bringing together of results from four different techniques in order to confirm details of material behavior that would have been inaccessible to any technique individually. The mechanical tests were used, along with fractographic and high-speed photographic observations, to validate and refine the modeling effort. This in turn has given unprecedented access to details of the deformation and damage processes occurring in the samples as a function of time, along with precise information concerning the accompanying stress levels.

3. Experimental and Modeling

3.a Experimental

Samples were prepared from the following materials, of widely different impedances, namely,

i) 13.96 mm thick alumina ceramic plate,

ii) either a 1.5 mm thick layer of Ethylene-propylene-diene monomer (EPDM) rubber or a 2.0 mm thick layer of expanded Teflon (a fluoro-polymer composite that consists of an expanded polytetrafluoroethylene (ePTFE) matrix filled with boron nitride (BN) particles), and

iii) 11.3 mm thick composite consisting of S2 glass fiber woven fabric (0.81 kg/m^2) in an SC15 epoxy resin, produced using the vacuum assisted resin transfer molding process.

These materials were used for individual layer tests or were assembled into 2- and 3-layer plates. Cylindrical samples 11.0, 15.7 or 19.0 mm in diameter were then core-drilled from the plates in the through-thickness direction and samples were compression tested at various nominal strain rates between 400 and 1200 s^{-1} using the SHPB (the compression axis normal to fiber plane). Rather than detail all the individual tests performed, this report will focus in particular on a limited series of tests which show the principal characteristics of SHPB test results of the components.

The particular SHPB apparatus used consists of Inconel 718 bars, a 356 mm long striker bar, 3450 mm incident and 1850 mm transmitter bars, all with a diameter of 19.05 mm. Further details of the experimental set-up and standard data reduction routines are available elsewhere [3]. During the data reduction, a dispersion correction was also applied for all the data sets. For dispersion correction, a routine developed in Center for Composite Materials, University of Delaware was used.

Since the strain levels during the ceramic testing are usually small (1-2 percent), the reflected pulse from the split Hopkinson bar is not capable of providing accurate strain measurement so reliable strain data has to be obtained by mounting strain-gages on the specimen surface. For this purpose, samples were fitted with strain gages, as shown in Fig. 1, so as to monitor real-time strains (and stresses) during the course of the tests. Strain gages with 0.79 mm element lengths were used generally,

although several tests were also carried out with an array of gages designed to sample the strain simultaneously at several locations along the sample length and thus provide a strain/time/position map of the wave passage. This is an important contribution for multi-layer material testing.

First, the single layer tests were performed for ceramic, composite, rubber and expanded Teflon samples. These results were used to provide data for, and check the validity of, the numerical model. Next, tests were performed on double layer, ceramic/composite samples. Finally, the three layer case was addressed where the different layers consisted of ceramic and composite with either a rubber or Teflon interlayer.

When a ceramic material is tested, the harder specimen will indent the end surfaces of the bars during loading. To minimize the problem of damaging the bars by indentation, disposable acoustic impedance matched Inconel 718 platens or WC were placed between the specimen and the bars.

At first when rubber and expanded Teflon were tested, lateral expansion of the material was permitted. However, in practical large-scale structures, the rubber and expanded Teflon interlayer would be constrained by the surrounding material and the effects of such lateral constraint on the resulting properties have to be considered. Severe lateral constraints would affect the through thickness stresses reported. Samples used in the SHPB testing can, at the most, have the same diameter as the bar and experiments show that considerable radial flow occurred in the rubber interlayer. In fact, the real case will probably lie somewhere between the extremes of completely constrained and completely unconstrained so the evaluation of both limiting cases is correspondingly important.

Consequently, some rubber and expanded Teflon samples were also subjected to lateral confinement by placing a 6 mm wide steel retaining ring around the junction of the sample as illustrated in Fig. 1 below. An interference fit was achieved between the specimen and the steel ring, and no material was squeezed out into the region between them while testing. Possible inertial effects and interactions between the ring and the other components of the sample were checked via tests on individual ceramic and composite samples with the ring in place. No modification to the wave propagation behavior was observed in the presence of the steel ring.

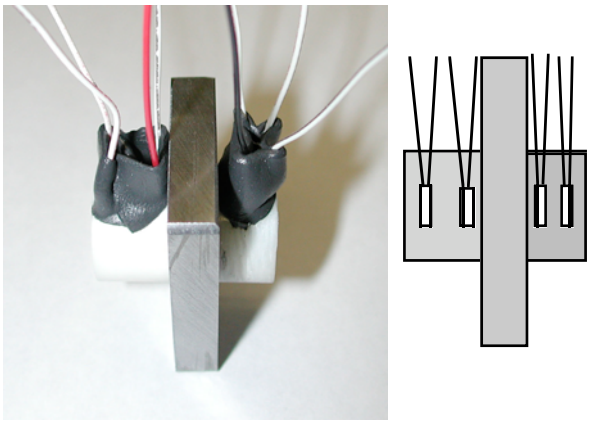

Fig. 1. Constrained 3-layer sample, actual photograph before testing, plus schematic. Note placement of strain gages.

3.b Modeling

As stated above, the desired ideal result is that data calculated from the model closely match output from the strain gages on the incident and transmitter bars, and on the sample itself. Similarly, the number and shape of ceramic fragments and the damage modes effective in the composite should also match the damage data calculated from the model. If all these conditions are met, it indicates that the model is accurately capturing the wave propagation behavior inside the sample and bars. The model can then be used with confidence to determine local conditions at any point within the sample: this information can be used, for example, to predict fracture initiation sites, local stress gradients and discontinuities. Fracture of composites and especially ceramics is highly statistical in nature and depends on the local population of defects so it cannot be expected that the model will *exactly* reproduce the actual fracture behavior since even small defects can influence damage initiation. Nevertheless, the main thrust of the present simulations is to understand when and where damage starts and to see how it propagates.

The JH-2 model [4-10] was used to simulate the damage evolution and dynamic failure of the ceramic. This is a pressure and strain-rate sensitive material model which, although developed for ballistic impact velocity range, has been successfully applied to relatively low impact velocities [11, 12]. The JH-2 model was proposed by Johnson and Holmquist [4, 6, 7] in order to improve the efficiency of a previous ceramic model which is referred to as JH-1. The constitutive behavior described by this

model as follows. There is an initial elastic regime which continues until yield occurs (the plastic strain starts at this point). Damage starts to accumulate and the material weakens. The material then behaves along the weakened material curve. The rate at which the material moves from undamaged to damaged and the strength of the weakened material are all variables. The model consists of a pressure and rate dependent strength model determined by accumulated effective plastic strain, and a polynomial equation of state. Dilatation is considered by transforming deviatoric energy to hydrostatic energy when the damage accumulates during the impact processes [13].

The strength model of JH-2 has the following normalized forms;

$$\sigma_i^* = A(P^* + T^*)^N (1 + C \ln \dot{\varepsilon}^*), \qquad \text{(Eqn. 1)}$$

for intact ceramics, and

$$\sigma_f^* = B(P^*)^M (1 + C \ln \dot{\varepsilon}^*), \qquad \text{(Eqn. 2)}$$

for fractured ceramics. In Eqs. 1 and 2, σ_i^*, σ_f^* are the normalized effective stresses for the intact and fractured ceramics, respectively. P^* is normalized pressure variable, T^* is normalized tensile strength. $\dot{\varepsilon}$ is normalized strain rate variable. They are normalized by $\sigma_i^* = \frac{\sigma}{\sigma_{HEL}}$, $P^* = \frac{P}{P_{HEl}}$, $T^* = \frac{T}{P_{HEl}}$, $\dot{\varepsilon}^* = \frac{\dot{\varepsilon}}{\dot{\varepsilon}_o}$,

in which σ_{HEL} and P_{HEL} are the effective stress and the pressure corresponding to the Hugoniot Elastic Limit (specific shock pressure below which the shock compressed material behaves elastically) (HEL) of the ceramic material. $\dot{\varepsilon}_o$ is a reference strain rate. *A, N, B, M, C*, $T, \dot{\varepsilon}_o$, σ_{HEL} and P_{HEL} are the parameters in the strength model.

The strength transition from intact to fractured material is controlled by a damage criterion which depends on accumulated effective plastic strain. The normalized effective stress for damaged ceramics is;

$$\sigma^* = \sigma_i^* - D(\sigma_i^* - \sigma_f^*), \qquad \text{(Eqn. 3)}$$

where D $(0 \le D \le 1)$ is the damage variable, which is expressed as

$$D = \sum \frac{\Delta \varepsilon^p}{\varepsilon_f^p}, \qquad \text{(Eqn. 4)}$$

where $\Delta\varepsilon^p$ is the effective plastic strain during a cycle of integration and $\varepsilon_f^p = f(P)$ is the fracture plastic strain under a constant pressure. Once the accumulated effective plastic strain reaches the fracture plastic strain, fully damage is resulted for the material. The expression of the fracture plastic strain has the following form;

$$\varepsilon_f^p = D_1(P^* + T^*)^{D_2}, \qquad \text{(Eqn. 5)}$$

where D_1 and D_2 are two damage constants. The material cannot undergo any plastic strain at $P^* = -T^*$, but ε_f^p increases as P^* increases.

Thus, the strength function of JH-2 can be reorganized as;

$$F(\sigma, p, D, \dot{\varepsilon}) = \sigma^* - \sigma_i^* + D(\sigma_i^* - \sigma_f^*) = 0, \qquad \text{(Eqn. 6)}$$

with the aid of a non-associated flow law, the incremental effective plastic strain can be obtained as;

$$d\varepsilon^p = \sqrt{\frac{2}{9}\left[\begin{array}{l}(d\varepsilon_{xx}^p - d\varepsilon_{yy}^p)^2 + (d\varepsilon_{xx}^p - d\varepsilon_{zz}^p)^2 + (d\varepsilon_{yy}^p - d\varepsilon_{zz}^p)^2 \\ + \\ \frac{3}{2}(d\gamma_{xy}^{p\,2} + d\gamma_{yz}^{p\,2} + d\gamma_{zx}^{p\,2})\end{array}\right]}, \qquad \text{(Eqn. 7)}$$

where $d\varepsilon_{xx}^p, d\varepsilon_{yy}^p, d\varepsilon_{zz}^p, d\gamma_{xy}^p, d\gamma_{yz}^p$ and $d\gamma_{zx}^p$ are incremental plastic strain during an integration cycle. In the present study, von-Mises yield function serves as the plastic potential function in the non-associate plastic flow.

A polynomial equation of state is employed in the JH-2 model. The pressure variable is calculated as,

$$P = k_1\mu + k_2\mu^2 + k_2\mu^3 + \Delta P, \qquad \text{(Eqn. 8)}$$

where k_1, k_2 and k_3 are constants (k_1 is the bulk modulus), μ is a compression variable, and $\mu = \frac{\rho}{\rho_o} - 1$ for current density ρ and initial density ρ_o. For tension with $\mu < 0$, the above equation is replaced by $P = k_1\mu.\Delta P$ in Eq. (8) is an additional incremental pressure determined from energy considerations to include the dilatation effect after compression failure. Details on the JH-2 ceramic material model are described in the literature [4, 6, 7].

It should be noted that the JH-2 model is a macro-scale material failure model and the parameters involved can be obtained from common quasi-static tests, split Hopkinson pressure bar tests, and plate impact tests, etc. They are, therefore, relatively easy to collect from the available literature. Recovered specimen shape after testing allows us to determine the dominant failure criterion during this kind of impact event. Simulation also allows us to understand the evolution of damage with time. In addition to the material constants, given in Table 1, the JH-2 model in LS-DYNA also includes a criterion for material erosion. The first option is based on a critical value of effective plastic strain, and the second on tensile failure. It must be emphasized that erosion criteria must be used with caution as early and premature erosion of material can lead to incorrect model predictions, and significantly increase the mesh-size dependency of the calculation. Damage initiates when the stress of the intact material exceeds the material strength at the current pressure. This leads to an increment of plastic strain and corresponding increase in damage. The erosion criterion is based on calculating when the total plastic strain exceeds a specified plastic strain. If any negative value is entered for the failure strain, element erosion occurs if the tensile pressure exceeds the specified maximum tensile pressure. In our studies, the failure strain erosion criterion was used and the erosion strain was 0.7. The values of equation of state (EOS) parameters were taken from Ref. [14]. Mesh and parameter sensitivity studies were both carried out, the material property data set given in Table 1 was found to be the optimum.

Table 1 JH-2 Parameters for Alumina

Parameter	Description	Value
ρ_o	Density	3.89 g/cc
G	Shear modulus	152 GPa
HEL	Hugoniot elastic limit	7.00 GPa
A	Intact strength constant	0.88
N	Intact strength constant	0.64
C	Strain rate constant	0.007
B	Fracture strength constant	0.45
M	Fracture strength constant	0.60
SFMAX	Max strength of failed mat'l / HEL stress	1.0
T	Tensile strength	0.462 GPa
K1	Pressure (EOS) constant	231 GPa
K2	Pressure (EOS) constant	-160 GPa
K3	Pressure (EOS) constant	2774 GPa
BULK	Bulking constant	1.0
D1	Damage constant	0.0125
D2	Damage constant	0.70

Failure modeling of composite materials under impact loading has been the subject of numerous studies, e.g., Abrate [15], Richardson and Wisheart [16], Choi and Chang [17] and Davies and Zhang [18]. SHPB has also been employed to study the dynamic properties of composites under compressive, tensile and shear loading conditions. Research efforts utilizing various versions of the SHPB to characterize dynamic properties of composites at high strain rates have been focused on specimen geometry effects, through thickness stitching effects, fiber orientation effects, and strain rate effects. However, few studies have been reported on modeling progressive failure in composites during Hopkinson pressure bar testing. In this chapter, a rate dependent progressive failure model was used to account for the nonlinear and rate dependent behavior commonly observed for fiber reinforced composite materials under high strain rate conditions. To model the progressive failure behavior of composite due to transverse impact, a composite lamina model, based on the 3D stress field that has been developed by Materials Sciences Corporation (MSC), was used. It has been implemented into LS-DYNA as MAT 161. The model with DMG option (MAT162) is a generalization of the basic layer failure model of MAT 161 by adopting the damage mechanics approach for characterizing the softening behavior after damage initiation. This failure model can be used to effectively simulate fiber failure,

matrix damage, and delamination behavior under all conditions - opening, closure, and sliding of failure surfaces.

Furthermore, this progressive failure modeling approach is advantageous as it enables one to predict delamination when locations of delamination sites cannot be anticipated; i.e., locations of potential delamination initiation are calculated without *a-priori* definition of an interlaminar crack surface. This failure model has been successfully utilized to characterize the impact damage in composite structures for a wide range of impact problems [19]

For this material model, the unidirectional layer failure criteria and the associated property degradation models are described as follows. Note that all failure criteria are expressed in terms of stress components based on ply level stresses (σ_a, σ_b, σ_c, τ_{ab}, τ_{bc}, τ_{ca}) with a, b and c denoting the finer, in-plane transverse and out-of-plane directions, respectively.

Three criteria are used for fiber failure, one in tension/shear, one in compression and another one in crushing under pressure. They are chosen in terms of quadratic stress forms as follows:

Tensile/shear fiber mode:

$$f_1 = \left(\frac{\langle \sigma_a \rangle}{S_{aT}} \right)^2 + \left(\frac{\tau_{ab}^2 + \tau_{ca}^2}{S_{FS}^2} \right) - 1 = 0 , \qquad \text{(Eqn. 9)}$$

compression fiber mode:

$$f_2 = \left(\frac{\langle \sigma'_a \rangle}{S_{aC}} \right)^2 - 1 = 0 , \; \sigma'_a = -\sigma_a + \left\langle -\frac{\sigma_b + \sigma_c}{2} \right\rangle \qquad \text{(Eqn. 10)}$$

Crush mode:

$$f_3 = \left(\frac{\langle p \rangle}{S_{FC}} \right)^2 - 1 = 0 , \; p = -\frac{\sigma_a + \sigma_b + \sigma_c}{3} . \qquad \text{(Eqn. 11)}$$

where $\langle\rangle$ are Macaulay brackets, S_{aT} and S_{aC} are the tensile and compressive strengths in the fiber direction, and S_{FS} and S_{FC} are the layer strengths associated with the fiber shear and crush failure, respectively.

Matrix mode failures must occur without fiber failure, and hence they will be on planes parallel to fibers. For simplicity, only two failure planes are considered: one is perpendicular to the

planes of layering and the other one is parallel to them. The matrix failure criteria for the failure plane perpendicular and parallel to the layering planes, respectively, have the forms:

Perpendicular matrix mode:

$$f_4 = \left(\frac{\langle \sigma_b \rangle}{S_{bT}}\right)^2 + \left(\frac{\tau_{bc}}{S'_{bc}}\right)^2 + \left(\frac{\tau_{ab}}{S_{ab}}\right)^2 - 1 = 0, \qquad \text{(Eqn. 12)}$$

parallel matrix mode (Delamination):

$$f_5 = S\left[\left(\frac{\langle \sigma_c \rangle}{S_{bT}}\right)^2 + \left(\frac{\tau_{bc}}{S''_{bc}}\right)^2 + \left(\frac{\tau_{ca}}{S_{ca}}\right)^2\right] - 1 = 0, \qquad \text{(Eqn. 13)}$$

where S_{bT} is the transverse tensile. Based on the Coulomb-Mohr theory, the shear strengths for the transverse shear failure and the two axial shear failure modes are assumed to be the forms,

$$S_{ab} = S_{ab}^{(0)} + \tan(\varphi)\langle -\sigma_b \rangle, \qquad \text{(Eqn. 14)}$$

$$S'_{bc} = S_{bc}^{(0)} + \tan(\varphi)\langle -\sigma_b \rangle, \qquad \text{(Eqn. 15)}$$

$$S_{ca} = S_{ca}^{(0)} + \tan(\varphi)\langle -\sigma_c \rangle, \qquad \text{(Eqn. 16)}$$

$$S''_{bc} = S_{bc}^{(0)} + \tan(\varphi)\langle -\sigma_c \rangle, \qquad \text{(Eqn. 17)}$$

where φ is a material constant as tan(φ) is similar to the coefficient of friction, and $S_{ab}^{(0)}$, $S_{ca}^{(0)}$ and $S_{bc}^{(0)}$ are the shear strength values of the corresponding tensile modes.

Failure predicted by the criterion of f_4 can be referred to as transverse matrix failure, while the matrix failure predicted by f_5, which is parallel to the layer, can be referred as the delamination mode when it occurs within the elements that are adjacent to the ply interface.

When fiber failure in tension/shear mode is predicted in a layer by f_1, the load carrying capacity of that layer is completely eliminated. All the stress components are reduced to zero quasi-instantaneously (100 time steps to avoid numerical instability). For compressive fiber failure, the layer is assumed to carry a residual axial load, while the transverse load carrying capacity is reduced to zero. When the fiber compressive failure mode is reached due to f_2, the axial layer compressive strength stress is assumed to be reduced to a residual value S_{RC} (=SFFC*S_{AC}). The axial stress is then assumed to remain constant, i.e., σ_a=-S_{RC}, for continuous loading, while the subsequent unloading curve follows a

reduced axial modulus to zero axial stress and strain state. When the fiber crushing failure occurs, the material is assumed to behave elastically for compressive pressure, $p > 0$, and to carry no load for tensile pressure, $p < 0$.

When a matrix failure (delamination) in the a-b plane is predicted, the strength values for $S_{ca}^{(0)}$ and $S_{bc}^{(0)}$ are set to zero. This results in reducing the stress components σ_c, τ_{bc} and τ_{ca} to the fractured material strength surface. For tensile mode, $\sigma_c > 0$, these stress components are reduced to zero. For compressive mode, $\sigma_c < 0$, the normal stress s_c is assumed to deform elastically for the closed matrix crack. Loading on the failure envelope, the shear stresses are assumed to 'slide' on the fractured strength surface (frictional shear stresses) like in an ideal plastic material, while the subsequent unloading shear stress-strain path follows reduced shear moduli to the zero shear stress and strain state for both τ_{bc} and τ_{ca} components.

The post failure behavior for the matrix crack in the a-c plane due to f_4 is modeled in the same fashion as that in the a-b plane as described above. In this case, when failure occurs, $S_{ab}^{(0)}$ and $S_{bc}^{(0)}$ are reduced to zero instantaneously. The post fracture response is then governed by failure criterion of f_5 with $S_{ab}^{(0)} = 0$ and $S_{bc}^{(0)} = 0$. For tensile mode, $\sigma_b > 0$, σ_b, τ_{ab} and τ_{bc} are zero. For compressive mode, $\sigma_b < 0$, σ_b is assumed to be elastic, while τ_{ab} and τ_{bc} 'slide' on the fracture strength surface as in an ideal plastic material, and the unloading path follows reduced shear moduli to the zero shear stress and strain state. It should be noted that τ_{bc} is governed by both the failure functions and should lie within or on each of these two strength surfaces.

Failure criteria based on the 3D stresses in a plain weave composite layer with improved progressive failure modeling capability have also been established following the same approach as that for the unidirectional model. Note that the fabric failure criteria are expressed in terms of stress components based on ply level stresses (σ_a, σ_b, σ_c, τ_{ab}, τ_{bc}, τ_{ca}) with a, b and c denoting the in-plane fill, in-plane warp and out-of-plane directions, respectively.

The fill and warp fiber tensile/shear failure are given by the quadratic interaction between the associated axial and shear stresses, i.e.

$$f_6 = \left(\frac{\langle \sigma_a \rangle}{S_{aT}} \right)^2 + \left(\frac{\tau_{ab}^2 + \tau_{ca}^2}{S_{aFS}^2} \right) - 1 = 0 , \qquad \text{(Eqn. 18)}$$

$$f_7 = \left(\frac{\langle \sigma_b \rangle}{S_{bT}}\right)^2 + \left(\frac{\tau_{ab}^2 + \tau_{ca}^2}{S_{bFS}^2}\right) - 1 = 0 \qquad \text{(Eqn. 19)}$$

where S_{aT} and S_{bT} are the axial tensile strengths in the fill and warp directions, respectively, and S_{aFS} and S_{bFS} are the layer shear strengths due to fiber shear failure in the fill and warp directions. These failure criteria are applicable when the associated σ_a or σ_b is positive. It is assumed $S_{aFS} = SFS$, and

$$S_{bFS} = SFS * S_{bT}/S_{aT} \qquad \text{(Eqn. 20)}$$

when σ_a or σ_b is compressive, it is assumed that the in-plane compressive failure in both the fill and warp directions are given by the maximum stress criterion, i.e.,

$$f_8 = \left(\frac{\langle \sigma'_a \rangle}{S_{aC}}\right)^2 - 1 = 0, \ \sigma'_a = -\sigma_a + \langle -\sigma_c \rangle \qquad \text{(Eqn. 21)}$$

$$f_9 = \left(\frac{\langle \sigma'_b \rangle}{S_{bC}}\right)^2 - 1 = 0, \ \sigma'_b = -\sigma_b + \langle -\sigma_c \rangle \qquad \text{(Eqn. 22)}$$

where S_{aC} and S_{bC} are the axial compressive strengths in the fill and warp directions, respectively. The crush failure under compressive pressure is

$$f_{10} = \left(\frac{\langle p \rangle}{S_{FC}}\right)^2 - 1 = 0, \ p = -\frac{\sigma_a + \sigma_b + \sigma_c}{3} \qquad \text{(Eqn. 23)}$$

A plain weave layer can fail under in-plane shear stress without the occurrence of fiber breakage. This in-plane matrix failure mode is given by;

$$f_{11} = \left(\frac{\tau_{ab}}{S_{ab}}\right)^2 - 1 = 0 \qquad \text{(Eqn. 24)}$$

where S_{ab} is the layer shear strength due to matrix shear failure.

Another failure mode, which is due to the quadratic interaction between the thickness stresses, is expected to be mainly a matrix failure. This through the thickness matrix failure criterion is

$$f_{12} = S^2\left[\left(\frac{\langle \sigma_c \rangle}{S_{cT}}\right)^2 + \left(\frac{\tau_{bc}}{S_{bc}}\right)^2 + \left(\frac{\tau_{ca}}{S_{ca}}\right)^2\right] - 1 = 0 \qquad \text{(Eqn. 25)}$$

where S_{cT} is the through the thickness tensile strength, and S_{bc}, and S_{ca} are the shear strengths assumed to depend on the compressive normal stress σ_c, i.e.,

$$\begin{bmatrix} S_{ca} \\ S_{bc} \end{bmatrix} = \begin{bmatrix} S_{ca}^{(0)} \\ S_{bc}^{(0)} \end{bmatrix} + \tan(\varphi)\langle -\sigma_c \rangle \qquad \text{(Eqn. 26)}$$

When failure predicted by this criterion occurs within elements that are adjacent to the ply interface, the failure plane is expected to be parallel to the layering planes, and, thus, can be referred to as the delamination mode. Note that a scale factor S is introduced to provide better correlation of delamination area with experiments. The scale factor S can be determined by fitting the analytical prediction to experimental data for the delamination area.

Similar to the unidirectional model, when fiber tensile/shear failure is predicted in a layer by f_6 or f_7, the load carrying capacity of that layer in the associated direction is completely eliminated. For compressive fiber failure due to by f_8 or f_9, the layer is assumed to carry a residual axial load in the failed direction, while the load carrying capacity transverse to the failed direction is assumed unchanged. When the compressive axial stress in a layer reaches the compressive axial strength S_{aC} or S_{bC}, the axial layer stress is assumed to be reduced to the residual strength S_{aRC} or S_{bRC} where S_{aRC} = SFFC* S_{aC} and S_{bRC} = SFFC* S_{bC}. The axial stress is assumed to remain constant, i.e., (σ_a=-S_{aCR} or σ_b=-S_{bCR}, for continuous compressive loading, while the subsequent unloading curve follows a reduced axial modulus. When the fiber crush failure is occurred, the material is assumed to behave elastically for compressive pressure, p > 0, and to carry no load for tensile pressure, p < 0. When the in-plane matrix shear failure is predicted by f_{11} the axial load carrying capacity within a failed element is assumed unchanged, while the in-plane shear stress is assumed to be reduced to zero.

For through the thickness matrix (delamination) failure given by equations f_{12}, the in-plane load carrying capacity within the element is assumed to be elastic, while the strength values for the tensile mode, $S_A^{(0)}$ and $S_T^{(0)}$, are set to zero. For tensile mode, $\sigma_c > 0$, the through the thickness stress components are reduced to zero. For compressive mode, $\sigma_c < 0$, σc is assumed to be elastic, while τ_{bc} and τ_{ca} 'slide' on the fracture strength surface as in an ideal plastic material, and the unloading path follows reduced shear moduli to the zero shear stress and strain state.

The effect of strain rate on the layer strength values of the fiber failure modes is modeled by multiplying the associated strength values by a scale factor S_{RT} as

$$S_{RT} = 1 + C_{rate} \ln \frac{\dot{\bar{\varepsilon}}}{\dot{\varepsilon}_0} \qquad \text{(Eqn. 27)}$$

where $\dot{\bar{\varepsilon}}$ is the effective strain rate for $\dot{\varepsilon}_0 = 1 s^{-1}$

Composite damage model MAT_COMPOSITE_DMG_MSC implemented in LS-DYNA 970 was used in the damage analysis of composite specimens. The properties of PW S2-glass/SC15 composites are given in Table 2.

Table 2 MAT 162 input for PW S2-Glass/SC15 composites.

MID	**RO, g/cm3**	**EA, GPa.**	**EB, GPa.**	**EC, GPa.**	**PRBA**	**PRCA**	**PRCB**
xx	1.85	24.1	24.1	8.0	0.12	0.173	0.173
GAB, GPa.	**GBC, GPa.**	**GCA, GPa.**	**AOPT**				
2.8	2.8	2.8	2.0				
XP	**YP**	**ZP**	**A1**	**A2**	**A3**		
0.0	0.0	0.0	1.0	0.0	0.0		
V1	**V2**	**V3**	**D1**	**D2**	**D3**		
0.0	0.0	0.0	0.0	1.0	0.0		
SAT, MPa.	**SAC, MPa.**	**SBT, MPa.**	**SBC, MPa.**	**SCT, MPa.**	**SFC, MPa.**	**SFS, MPa.**	**SAB, MPa.**
586	345	586	345	55.2	850	241	48.3
SBC, MPa.	**SCA, MPa.**	**SFFC, MPa.**	**AMODEL**	**BETA**	**PHIC**	**E_LIMT**	**S_DELM**
48.3	48.3	0.3	2.0	0/90	40.0	0.6	1.4
OMGMAX	**ECRSH**	**EEXPN**	**CR1**	**AM1**			
0.996	0.01	3.0	0.0	4.0			
AM2	**AM3**	**AM4**	**CR2**	**CR3**	**CR4**		
4.0	2.0	2.0	0.0	0.0	0.0		

The Inconel bars were modeled with an isotropic elastic material model. The model and material constants for bars and rubber are given in Refs [1, 2, 20].

4. Results and Discussion

As mentioned above, rather than present details of all the experiments carried out, mainly those conducted with an incident bar velocity of 20.5 m/s will be described, unless otherwise stated, because this is the velocity at which significant damage began to appear in the individual layers of the composite backing plate. It was anticipated, therefore, that much of the ceramic and rubber deformation could be modeled as inelastic deformation. The composite portions began to exhibit delamination and other damage modes and an investigation of damage in this layer is also reported in this chapter. SHPB tests and simulations were performed for single-layer ceramic and composite cases, and both 2- and 3-layer situations, i.e., without and with a rubber interlayer respectively. As usual, the primary data for each test consist of i) experimental output from the SHPB bars, ii) numerical data which are then compared with the corresponding experiments. Tested specimens were subjected to fractographic examination. High-speed photography was used to record the deformation and/or fracture processes which were then compared with model predictions.

In order to confirm the validity of the ceramic constants used in Table 1 for the JH-2 model, a plate impact experiment was simulated and compared with experimental data. In such a test, the stress state is triaxial while the strain state is nearly one-dimensional. Grady [21] conducted a series of plate impact test experiments for alumina and Fig. 2 shows Grady's measured and our computed velocity/time histories at the Al_2O_3 sample and window interface using the ceramic constants of Table 1.

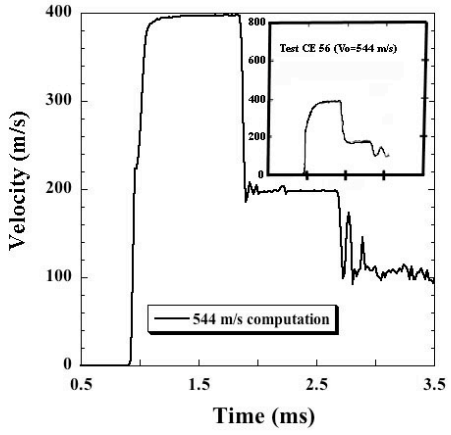

Fig. 2 Experimental (from [21]) and computational results for plate impact test on alumina.

In this symmetrical plate impact test, target and impactor were both Al_2O_3, the impactor plate was 5.0 mm thick with an 8.0 mm thick polyurethane foam (PF) backer. The target plate was 10.0 mm thick with a 25.4 mm thick LiF window and the impact velocity was 544 m/s. The computed results are in excellent agreement with the experimental data, confirming the proper selection of parameters for the JH-2 model.

4.a Ceramic Sample

SHPB tests and simulations were first performed for the ceramic only case. The specimens were typically 11.34 mm in diameter and 13.82 mm in length. The dimensions of the striker bar used are 100 mm in length and 19 mm in diameter. Dynamic experiments were conducted at a striker bar velocity of 30 m/s on the SHPB. In the damage analysis of a ceramic specimen, the full-symmetric numerical model was used with appropriate boundary conditions. The mesh includes a total of 321000 elements; 81000 elements for the specimen and 120000 elements for each of the incident and transmitter bars. Figs. 3 (a)&(b) show a comparison of the experimental and numerical simulation results for the ceramic sample and represent data from strain gages mounted on the incident and transmitter bars. The data match closely, showing that numerical simulation accurately captures the details of wave propagation.

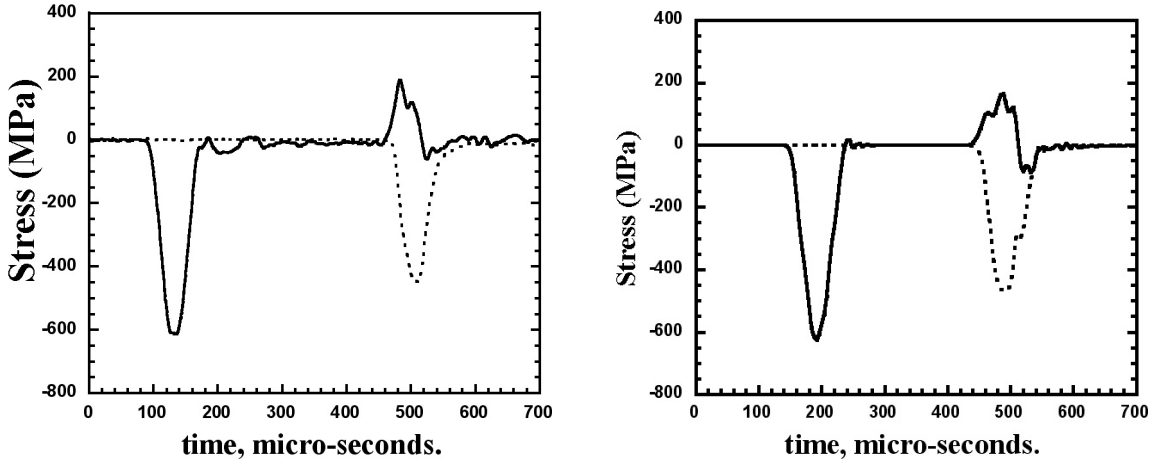

(a) (b)

Fig. 3 a) Experimental and b) calculated output from strain gages on the incident and transmitter bars during a test on a ceramic sample.

Figs. 4 (a)&(b) show the axial cross-sectional view and the top view of the recovered specimen.

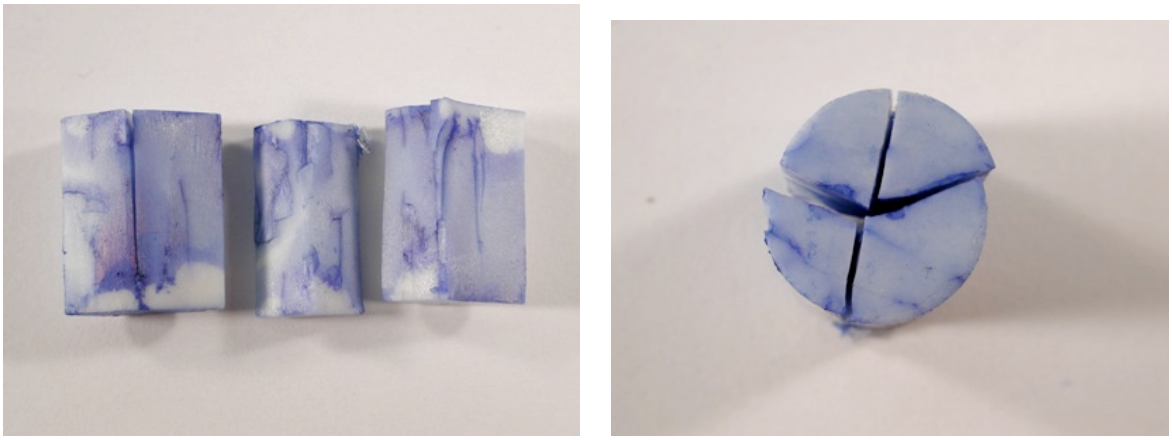

(a) (b)

Fig. 4 (a) Axial cross-sectional and (b) top views of the recovered ceramic specimen. (Sample infiltrated with blue dye to highlight cracks.)

Inspection of the axial cross-sectional and top views indicates that the specimen was fragmented and broken into approximately four major fragments. Ceramic fails in compression via the nucleation, growth and coalescence of (roughly) axially oriented microcracks. Even though the applied principal stresses of different magnitudes are compressive, local tensile stresses develop near inhomogeneities and crack tips within the specimen [22]. As the axial stress approaches the compressive strength, the crack density in the specimen reaches a critical value, where the cracks begin to interact at or near stress concentrations. The cross section in Fig. 4 shows there are several axial cracks causing axial splitting of the specimen.

Fig. 5 shows the numerical results for damage propagation for the ceramic sample between 324 and 344 μsec. This figure contains the specimen and two different cross-sectional views of the specimen which are normal and parallel to specimen axis, respectively. For this sample, damage initiates at the front surface (at 328 μsec) and the damage front propagates from front to back. Meanwhile damage also initiates at the front face and propagates inside the specimen. Eventually the damage fronts propagating inside the specimen meet and damage accumulation starts in the lower part of the specimen, forming major lines of damage progression, inclined to the axis of loading. The first signs of damage observed on the surface begin from the front surface and are propagating during the impact event. Axial splitting can readily be seen and then fragmentation occurs, generating numbers of fragments that are quite consistent with the evidence of Fig. 4.

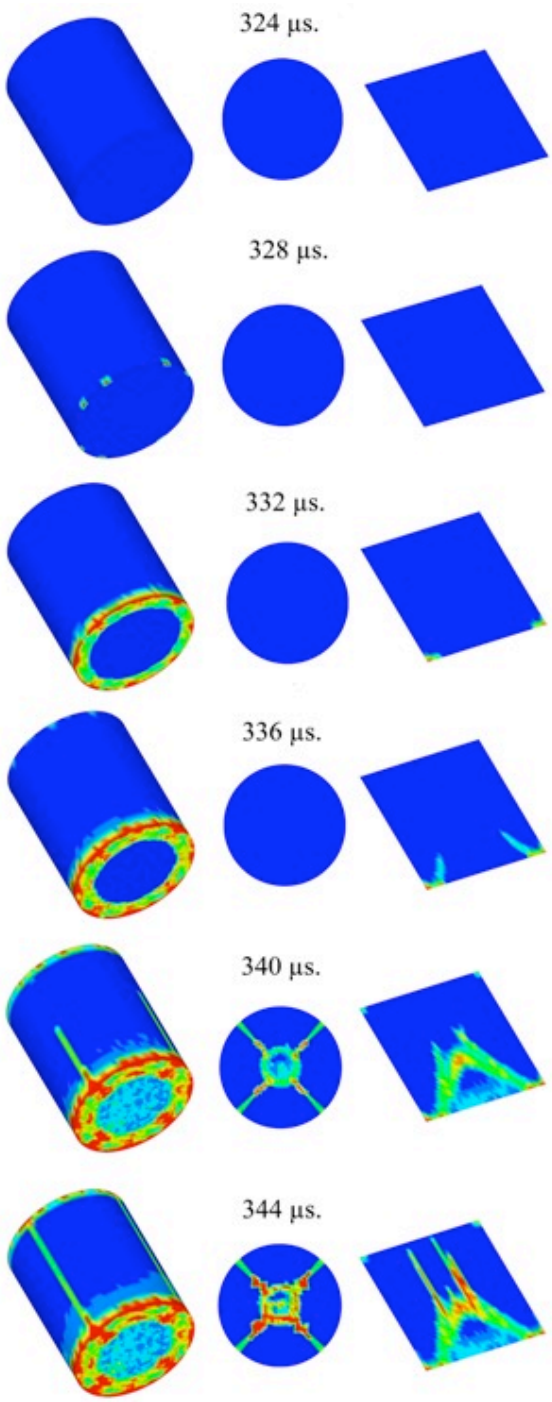

Fig. 5 Damage distribution diagram in a ceramic specimen.

4.b Composite Sample

Compressive properties and failure analysis of simple plain weave S2-glass/SC15 composites under high strain rate loading have been investigated in this section. A systematic experimental and numerical approach has been adopted to identify the damage progression at various stress levels and the strain rate effects on composites. High strain rate tests, at varying strain rates

between 595-1500 s^{-1}, were conducted on cylindrical samples, 11.5 and 11.3 mm in length and diameter respectively using the SHPB setup. Multiple loading of the sample in SHPB was avoided by using a transmitter bar shorter than the incident bar. This facilitates identification of the microstructural damage progression during the loading period. Several interrupted, high strain rate compression tests were also conducted to allow evaluation of deformed microstructures at a series of increasing strains. Maraging steel collars were used to limit the maximum strain response as shown in Fig. 6. Following testing, interrupted and fully loaded test samples were longitudinally sectioned and evaluated with optical and scanning electron microscopy. Typical damage mechanisms operative prior to and during failure were determined using high speed photography.

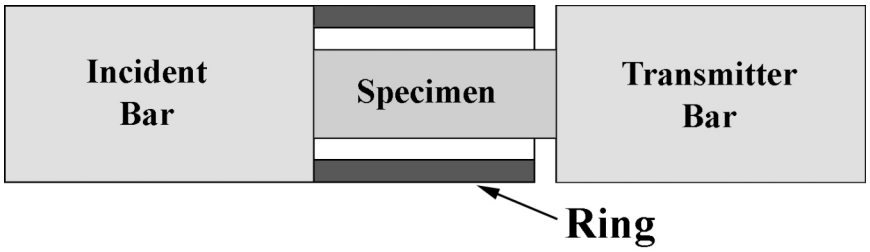

Fig. 6 Test configuration of interrupted dynamic test.

Figs. 7 (a) & (b) show typical sets of reflected and transmitted signals from SHPB experiments on the composite specimen along the through thickness direction at dynamic strain-rates in the range of 595-1500 s^{-1}. Experimental data have been grouped into two to show the cumulative effect of damage on the reflected and transmitted signal shapes.

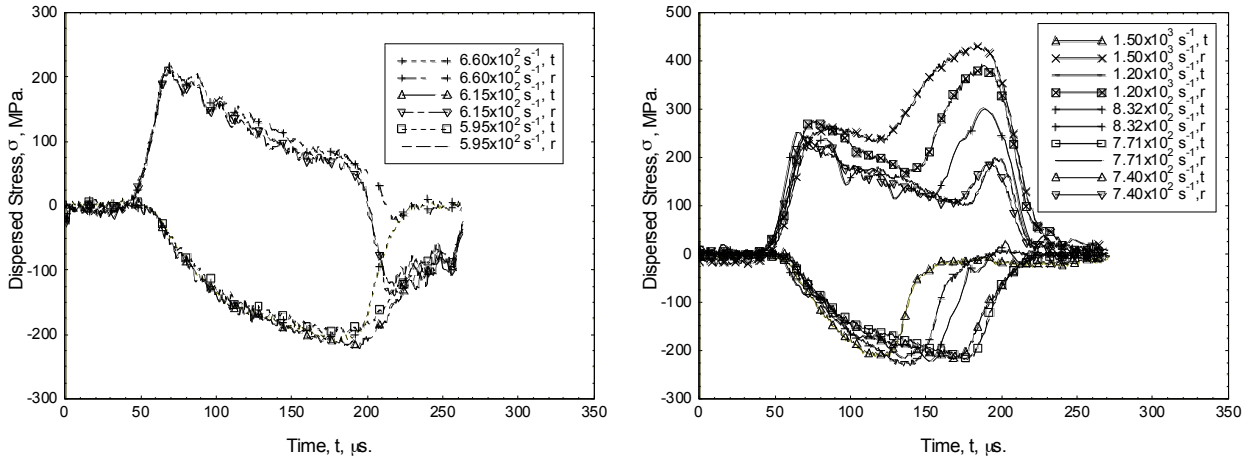

Fig. 7 Experimental bar output from strain gages on the incident and transmitter bars of a composite specimen at various strain rates.

According to classical 1-wave analysis, the reflected pulse gives information of the deforming specimen at the front surface (incident bar – specimen interface) and the corresponding strain rate of the specimen. However, the transmitted pulse gives information of the deforming specimen at the back surface (specimen – transmitter bar interface) and the average stress in the specimen.

Figs. 8 (a) and (b) show two different sets of strain-strain rate curves. For a wide range of striker bar velocities used, the strain rate is found to be a function of strain in the specimen. Since strain rate is a function of strain, a strain averaged strain rate (ASR) can be defined as:

$$\dot{\varepsilon}_{avg} = \frac{1}{\varepsilon_2 - \varepsilon_1} \int_{\varepsilon_1}^{\varepsilon_2} \dot{\varepsilon} . d\varepsilon \qquad \text{(Eqn. 28)}$$

where $\dot{\varepsilon}_{avg}$ is defined in the strain range, $\varepsilon_1 \le \varepsilon_s \le \varepsilon_2$. A strain averaging window is defined in the range, $0.02 \le \varepsilon_s \le 0.08$.

In Fig. 8 (a), strain rate increases with time from zero to a maximum value, and then decreases with time. On the other hand in Fig. 8 (b), strain rate increases as a function of time from zero to a certain value, and then forms a valley. After this, strain rate again increases with time and takes a sharp rise, indicating that the specimen has been extensively damaged or has failed. The incident bar end-specimen face encounters much less resistance from a damaged/failed specimen, resulting in a much faster bar end-face velocity, as indicated by the sharp rise in the reflected signal.

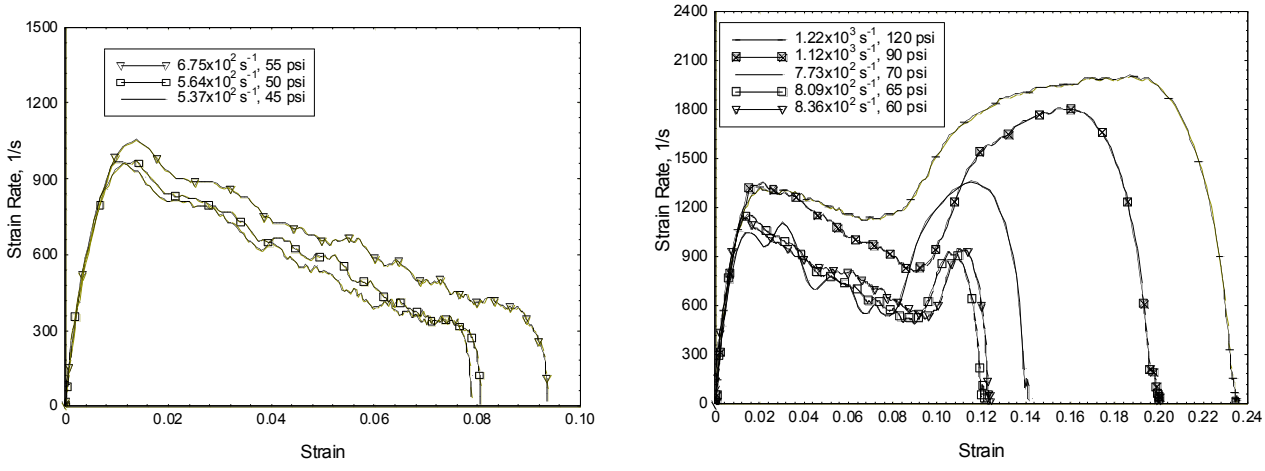

(a) (b)

Figure 8 Strain rate-strain response of plain weave S2-glass/SC15 composites in thickness direction: a) ASR = 537-675 s^{-1}; b) ASR = 809-1220 s^{-1}.

The axial force history on the front end that was in contact with the incident bar, F_1, was calculated from the difference between the incident and reflected pulses, and the transmitted pulse gave the force history on the back end that was in contact with the transmission bar, F_2, based on the one-dimensional wave theory,

$$F_1 = AE(\varepsilon_i + \varepsilon_r) \qquad \text{(Eqn. 29)}$$

$$F_2 = AE\varepsilon_t \qquad \text{(Eqn. 30)}$$

where F_1 and F_2 are axial forces at the front end and the back end of the specimen. The proximity to equilibrium can be evaluated by considering the parameter

$$R(t) = \left|\frac{\Delta\sigma(t)}{\sigma_{avg}(t)}\right| = 2\left|\frac{F_1 - F_2}{F_1 + F_2}\right| \qquad \text{(Eqn. 31)}$$

where $\Delta\sigma$ and σ_{avg} are difference and average value between the stresses at both end of specimen, respectively.

Fig. 9 (a), corresponding to the specimen tested at average dynamic strain rate of 537 s^{-1}, shows that the front and rear forces are very close throughout the loading history, apart from a brief peak at the top of the strain rate rise. Fig. 9 (b), from a test at an average strain rate of 1120 s^{-1}, shows a rather greater force difference at the initial rise (note the change of scale for 'R'), with a significant gap persisting over the rest of the loading time. Figures 9 (a) and (b) also show the proximity to equilibrium calculated indicating that especially at high testing pressures it is almost impossible to obtain stress equilibrium in the specimen.

The compressive stress–strain curves for this composite material along the through thickness direction at average dynamic strain-rates in the range of 537-1120 s^{-1}, are shown in Figure. 10.

The dynamic compressive stress–strain curves of the composite material along the through thickness direction initially show a nearly linear behavior at small strains (" < 2%) and then become nonlinear as the strain increases. The nearly linear initial portions of the stress–strain curves indicate that the composite is linearly elastic, without any damage at small strains. The nonlinear behavior at larger strains may indicate stress-induced damage and its accumulation with increasing strain, as

reflected by the decreasing slope of the stress–strain curves. Furthermore, the compressive stresses at some fixed strain are slightly, but nonlinearly, sensitive to strain rate in dynamic groups. Some of the specimens failed during experiments, except for the ones tested at strain rates of 675 s^{-1} and lower where unloading had started before failure occurred. Figure 9 also indicates that the maximum engineering strain before failure of the composite specimen along the through-thickness direction is approximately 8-9 %, which corresponds to a maximum engineering stress of 700 MPa.

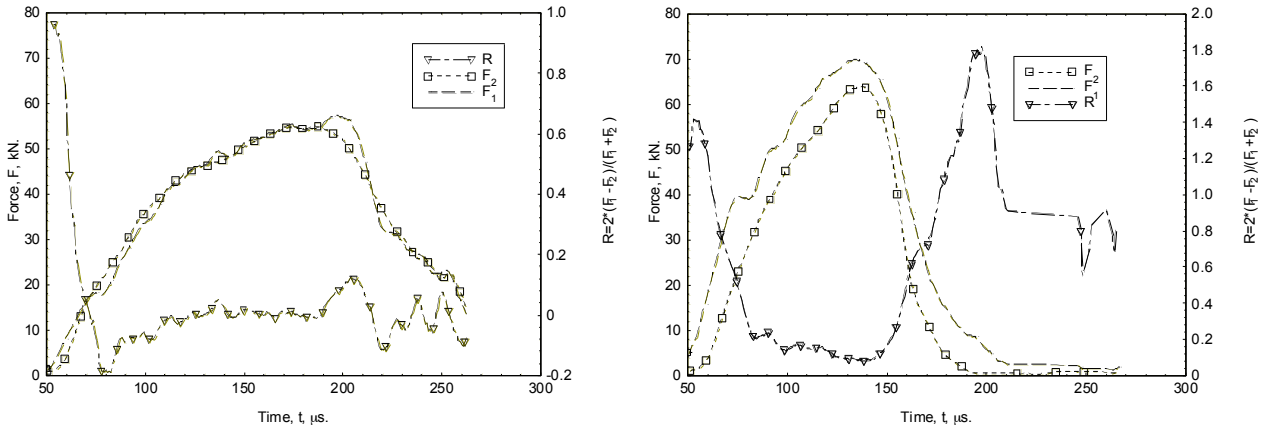

Fig. 9 Force history and dynamic equilibrium process in the composite specimen tested at an average strain rate of: a) 537 s^{-1} and b) 1120 s^{-1}.

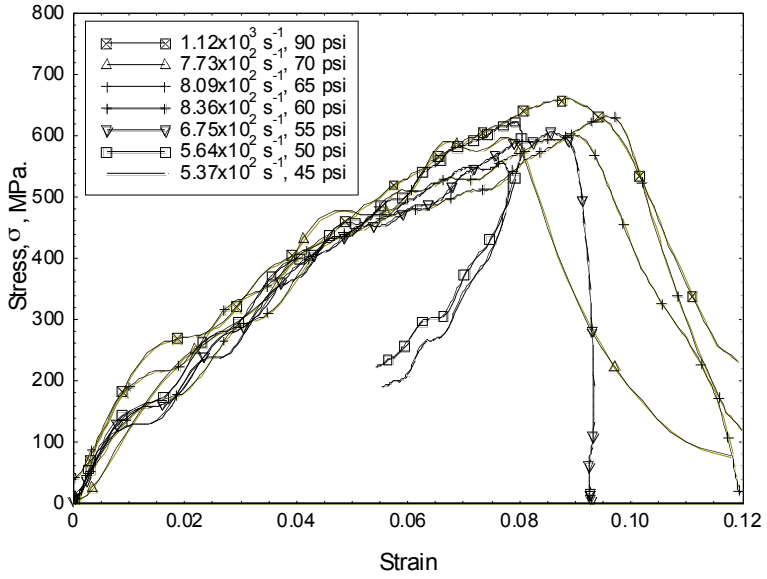

Fig. 10 Compression stress-strain curves of the composite in through thickness direction at different strain rates.

To study damage evolution in the samples, a high-speed camera Ultra 8, was used to record the SHPB tests. The propagation of damage (or fracture process) was observed by photographing the specimen sequentially in predetermined short time intervals (of the order of few μsec) using the high speed camera. With the Ultra 8 high speed camera used for the present study, a maximum of eight frames can be photographed in the speed range of 500 to 100 million frames per second. In the time domain, this implies that the interframe time can be varied between 10 nsec to 1 msec. The camera can be synchronized with the incident bar strain-gage or can be delayed to photograph the events of interest only.

Some evidence of the initiation and propagation events is available from high-speed photography of high strain rate loading. Photographs taken at 28 μsec intervals showed that damage can be visually observed when the stress in the sample nears the peak value, and visible damage propagates across the sample as the sample unloads.

Figs. 11 (a) to (c) show the high speed photographs of a series of tests all of which were conducted with striker bar velocities of 13, 15 or 20.5 m/s: these velocities would generate average strain rates of ~537, 675 & 809 s^{-1} respectively.

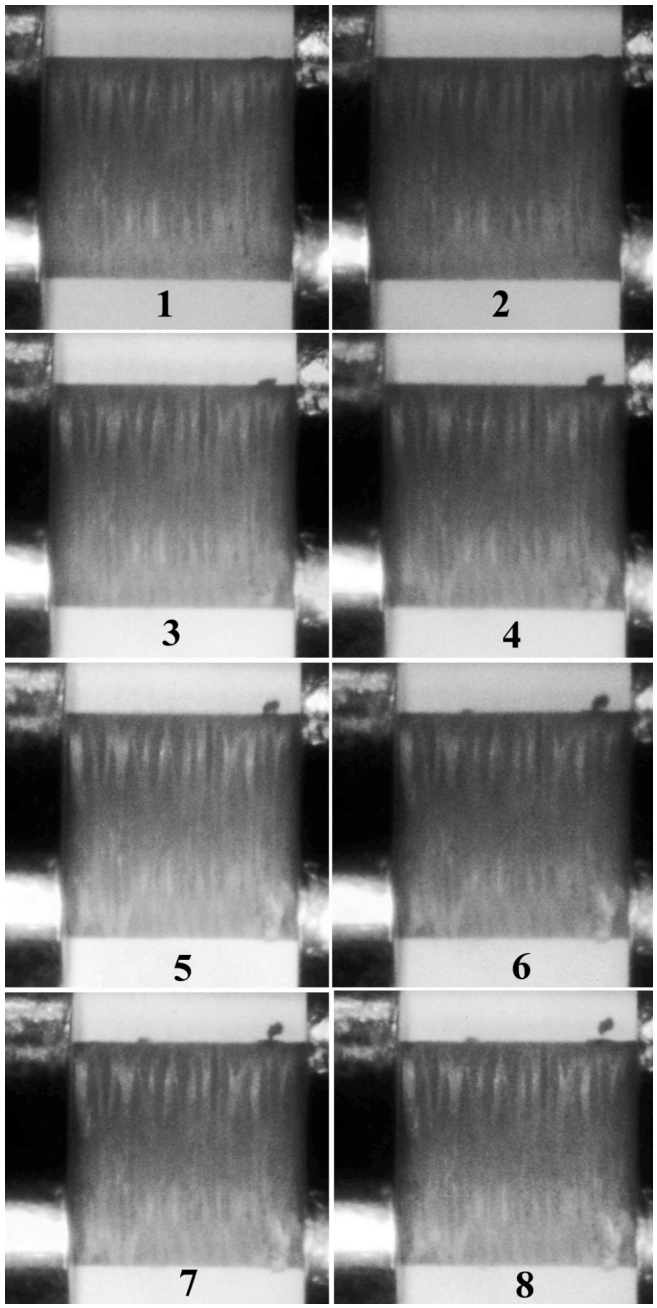

Fig. 11(a) High-speed photography of real time deformation of a composite specimen tested at an average strain rate of 537 s^{-1}. Interframe time 28 μs, exposure time 2 μs.

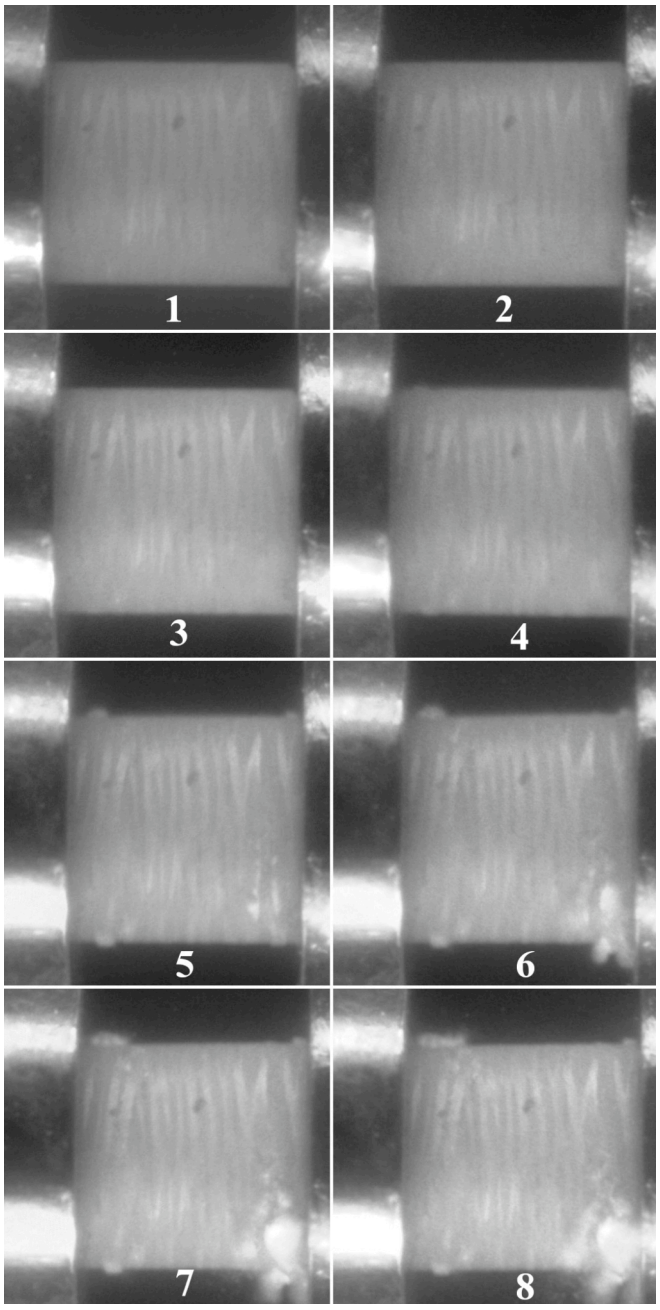

Fig. 11(b) High-speed photograph of real time deformation of a composite specimen tested at an average strain rate of 675 s^{-1}. Interframe time 28 μs, exposure time 2 μs.

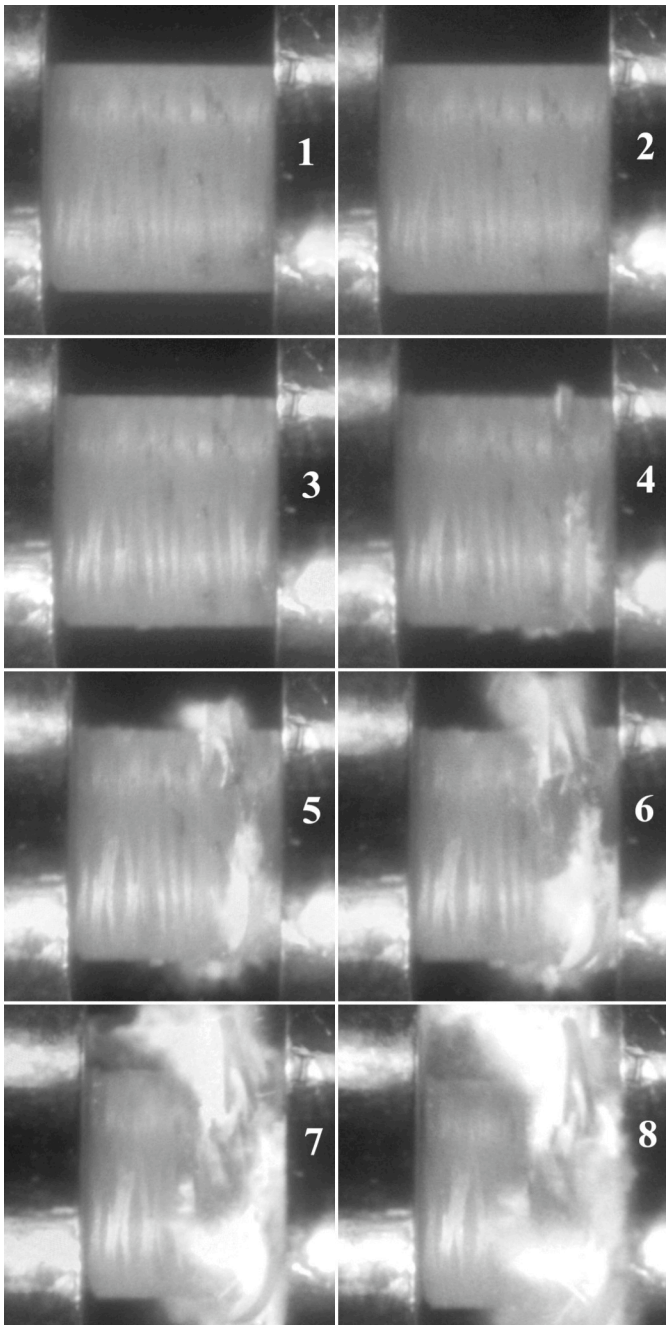

Fig. 11(c) High-speed photograph of real time deformation of a composite specimen tested at an average strain rate of 809 s^{-1}. Interframe time 28 μs, exposure time 2 μs.

The development of damage under impact was observed in real time. Fig. 11 (a) shows a typical sequence of real-time photographs of deformation of a composite specimen at an average strain rate of 537 s^{-1}. As can be seen from the figure, the response was principally elastic, consisting mainly of loading and unloading. A very minor fragment can be seen escaping from the top right of the sample and corresponds to the ejection of a small amount of matrix or fragment of a "cell" sectioned by the core drilling process. As the impact velocity and the average strain rate were increased, the damage content was also increased in the composite layer. Fig. 11 (b) shows that damage was highly localized at both specimen ends especially the region close to the specimen/transmitter bar interface was severely damaged when compared to the other regions. Fig. 11 (c) is clear experimental evidence showing how damage occurred and propagated inside the specimen. As the material was subjected to compressive loading along the thickness direction, the fiber yarns underwent extension in the transverse direction due to Poisson's effect. Fibers failed at different positions (localized around the specimen/transmitter bar interface) reaching failure limits in tension. Matrix material in and around the fiber yarns also developed cracks due to fiber failure. Stress redistribution occurred among intact fibers and resulted in higher stresses. Fiber pullout occurred when the matrix cracks propagated within the yarn. There is a significant temperature rise during impact and the fractured parts had a distinct smell of burned resin. The high speed photographs also appear to show fumes coming from the specimen surface. This suggests that heat generated during deformation could possibly contribute to the failure mechanism.

Interrupted testing was conducted to construct damage evolution history data by deforming specimens to prescribed strain levels. Five different lengths of maraging steel collars, the thicknesses of which were 11.14, 10.86, 10.67, 10.46 and 10.22 mm, were used and the anticipated strain values in the specimen are 1.8, 4.3, 5.9, 7.8 and 9.9 % respectively.

Figure 12 shows photographs of compressed composite samples in the through thickness direction at various strains.

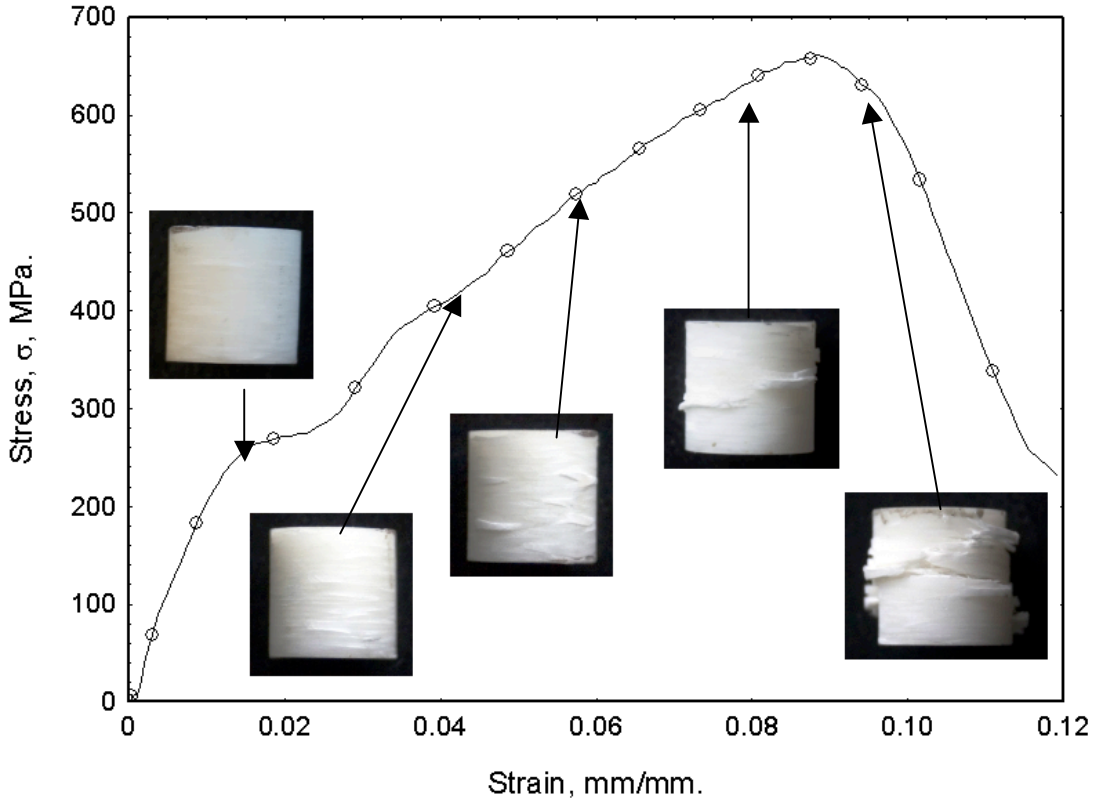

Fig. 12 Photographs of the specimens tested in the through thickness direction at various strains.

The compressive stress-strain curves for this composite material along the through thickness direction present a linear behavior at small strains, as shown in Figure 12. For lower strain values, i.e., less than 2%, no visible damage was detected on the lateral surface of the specimen and stress-strain curve shows a nearly linear behavior. After 4% strain, matrix cracking takes place in some of the transverse fibers, which appeared as discoloration/whitening at the fiber-matrix interfaces, which eventually results in some delamination, as reflected by the decreasing slope of the stress-strain curve. Such delamination causes the transverse fibers to be extruded from the lateral surface of the specimen. Extensive cracking has occurred at interlaminar boundaries, resulting in adjoining layers being displaced and squeezed out in different directions. At higher rates and stress levels catastrophic disintegration of the specimen is observed. Once the stress reaches its maximum value at around 700 MPa, the curve suddenly drops. This particular pattern of the stress-strain behavior indicates failure of the specimen, since only the free surface created in the specimen can only cause such sharp drop in the amplitude of the pulse.

Numerical simulations were also carried out using a newly developed damage model, namely MAT 162, which has been incorporated into LS-DYNA by CCM. This model uses damage mechanics principles for progressive damage and material degradation. In the damage analysis of a composite specimen, full-symmetric numerical model was used with appropriate boundary conditions. The mesh includes total 292800 elements; 52800 elements for the specimen and 120000 elements for each of the incident and transmitter bars. The composite specimen was modeled with 44 layers of elements in the thickness direction. Eroding single surface contact was defined between the bar ends and the composite specimen. The goals of the SHPB simulation were to match the bar response and the initiation and progression of the damage in the composite layer. Figures 13 (a) & (b) show the numerical and experimental results for the composite sample. The striker bar velocity was 18.2 m/s.

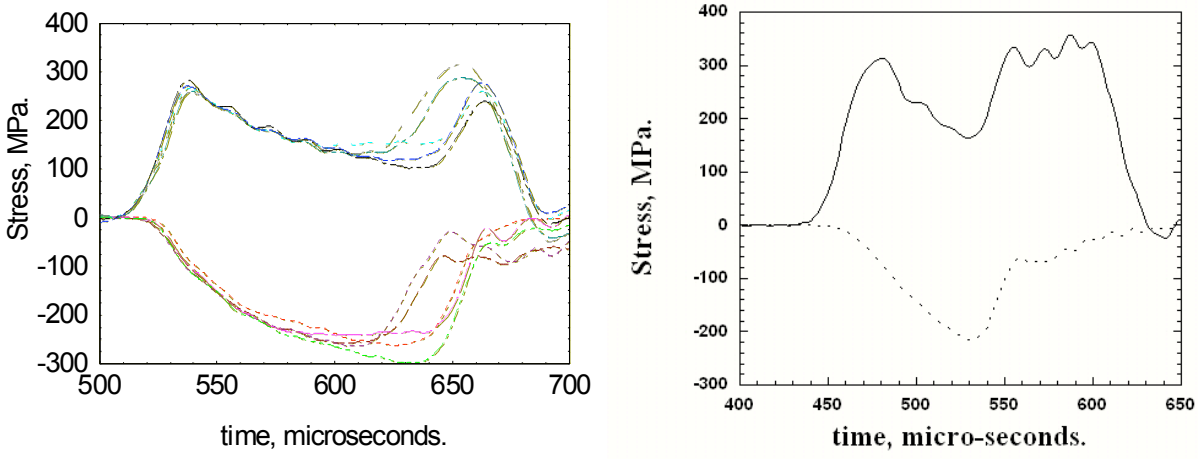

(a) (b)

Fig. 13 a) Experimental and b) calculated output from strain gages on the incident and transmitter bars during a test on a ceramic sample.

Figure 13 (a) shows the experimental results of five different specimens tested at identical test conditions. Experimental data show the increase of the reflected wave as a function of time from zero to a certain value, and then a valley formation, and after this a sharp rise occurs, indicating that the specimen has been extensively damaged or has failed. Up to valley formation point, all the specimens show similar behavior but when the disintegration begins different unloading behaviors are observed. Fracture of composites is highly statistical in nature and depends on the local population of defects and the location of the unit cells within the specimen so it cannot be expected that the model will exactly

reproduce the actual fracture behavior since even small defects can influence damage initiation. Nevertheless, the main thrust of the present simulations is to understand when and where damage starts and to see how it propagates. Generally, the numerical data show broadly similar behavior to the experimental data,

Fig. 14 shows the recovered specimen after the test. Extensive cracking has occurred at interlaminar boundaries, resulting in adjoining layers being displaced and squeezed out in different directions and giving rise to a dovetail appearance. Cracks initiate between the fiber layers and also progressive shear cracks were observed in the matrix.

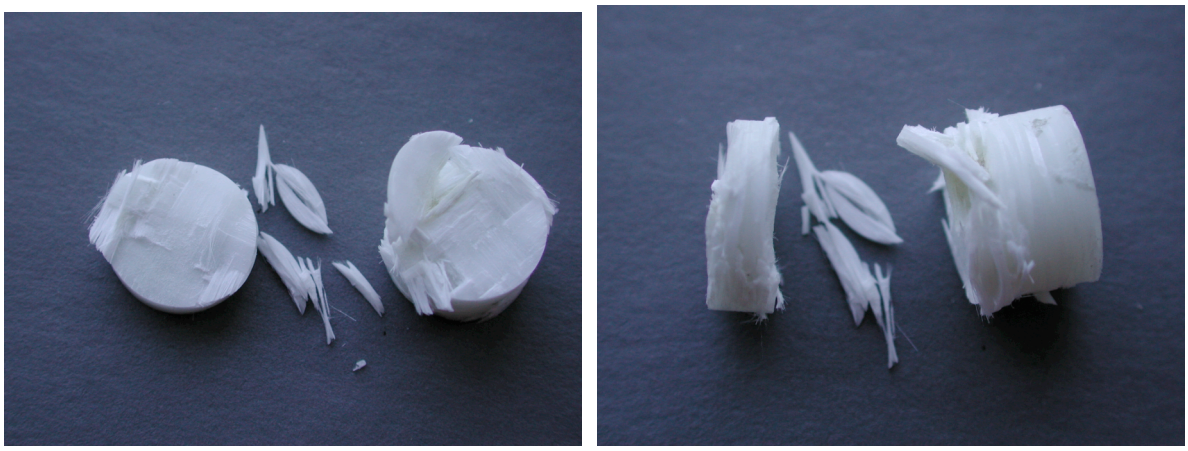

Fig. 14 Top and side views of the composite sample after testing at 18.2 m/s.

Contours of perpendicular matrix damage (matrix cracking) for composite are shown in Fig. 15. Numerical simulation shows compressive failure in the form of massive matrix cracks and fiber breakage at transmission face of the specimen, which matches well the real observed damage modes. The longitudinal compressive strain generates lateral strain which promotes the development of interlaminar matrix cracks. Fiber bundles flow outward from the specimen and eventually the specimen disintegrates catastrophically.

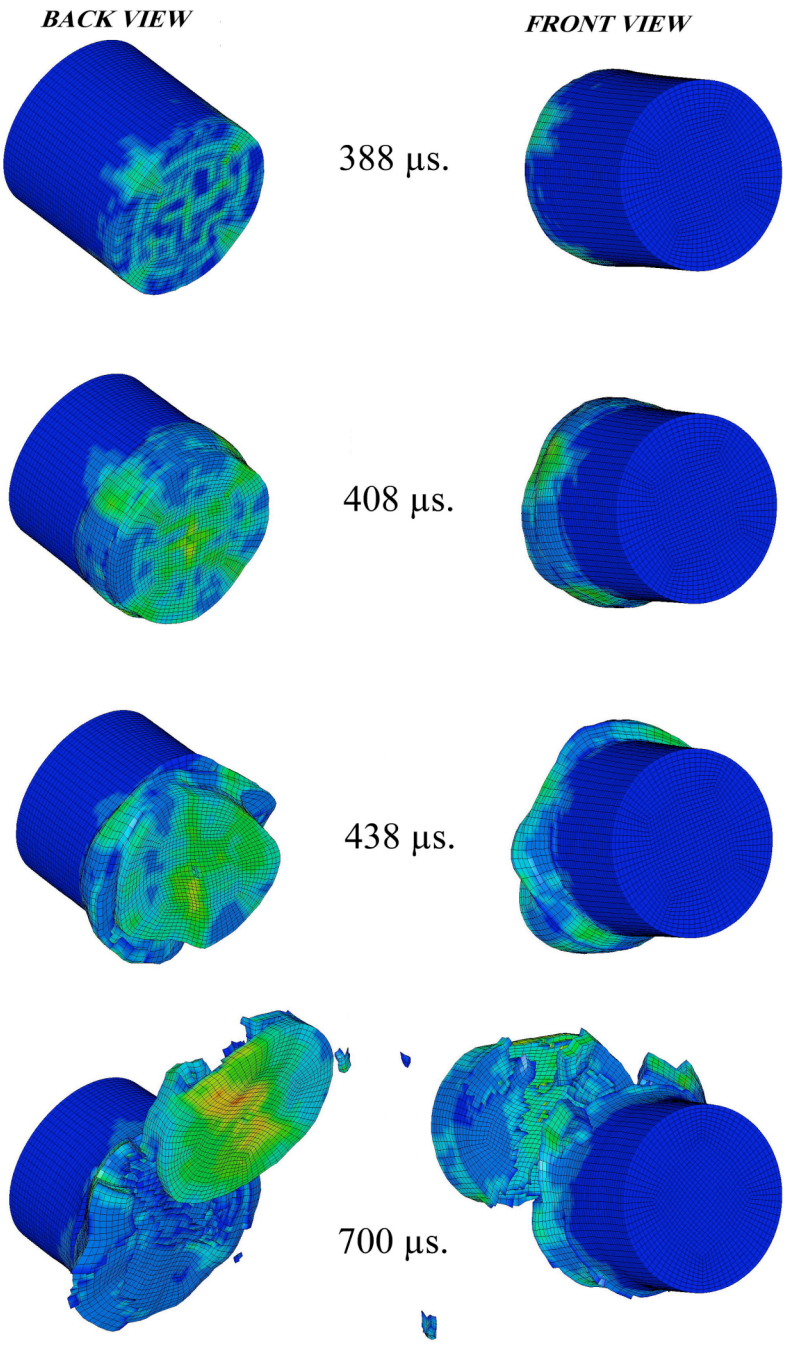

Fig. 15 Contours of perpendicular matrix damage.

4.c 2-layer Ceramic/Composite Sample

It is useful to continue by considering the behavior of a simple 2-layer, ceramic/composite sample tested at 20.5 m/s, Figs. 16 (a) & (b) show experimental and calculated data from the Hopkinson bars. The data match closely, showing that numerical simulation accurately captures the details of wave propagation. The pseudo-stress/strain curve for this test showed a steadily rising response indicating

that, although comprising two different materials, the sample behaved, to a first approximation, as a homogeneous sample the properties of which were dominated by the response of the lower modulus glass/epoxy composite.

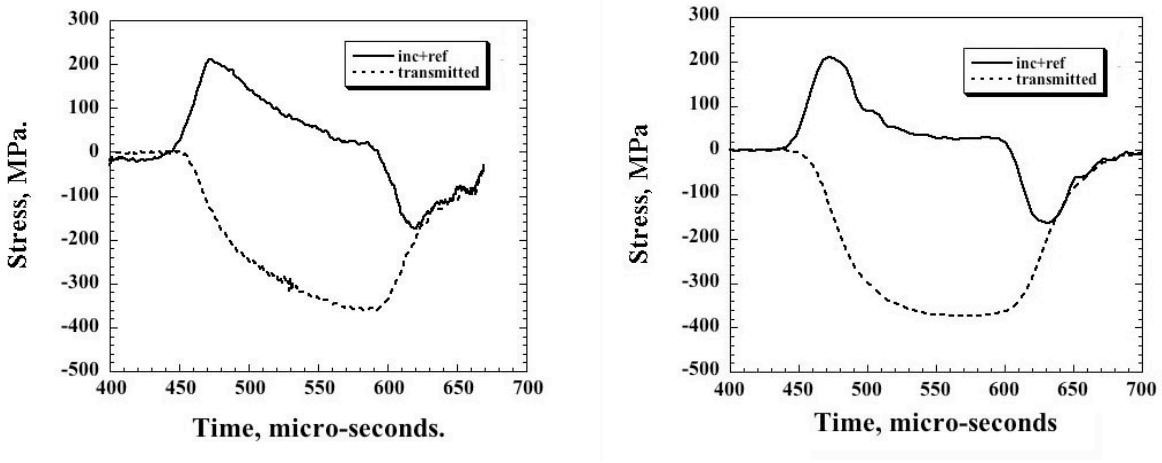

(a) (b)

Fig. 16 a) Experimental and b) calculated output from strain gages on the incident and transmitter bars during a test on a two layer, ceramic/composite, sample.

Fig. 17 shows the evolution with time of the z-stress at the centerline of the sample as a function of normalized sample length, where 0 is the incident bar/ceramic interface and 1 is the composite/transmitter bar interface. This figure permits a graphical understanding of the processes of wave transmission and clearly shows that during Hopkinson bar testing of multilayer materials, stress is not distributed uniformly inside the specimen. The one dimensional stress state usually assumed for conventional SHPB testing is inapplicable and it is clear that, even for a two-layer material, both numerical and experimental results have to be coupled for a complete understanding of the wave propagation.

During testing at high velocities, the ceramic frequently shattered, and various damage modes were activated in the composite. Examination of tested samples confirmed the general trends suggested by the mechanical property data. Fig. 18 shows a ceramic/composite sample after testing at 20.5 m/s in which severe damage has occurred in the ceramic. This figure shows that the dominant fracture mode is one of longitudinal splitting with the generation of, typically, 6 to 12 major fragments. Smaller debris particles arise due to further comminution of the principal fragments.

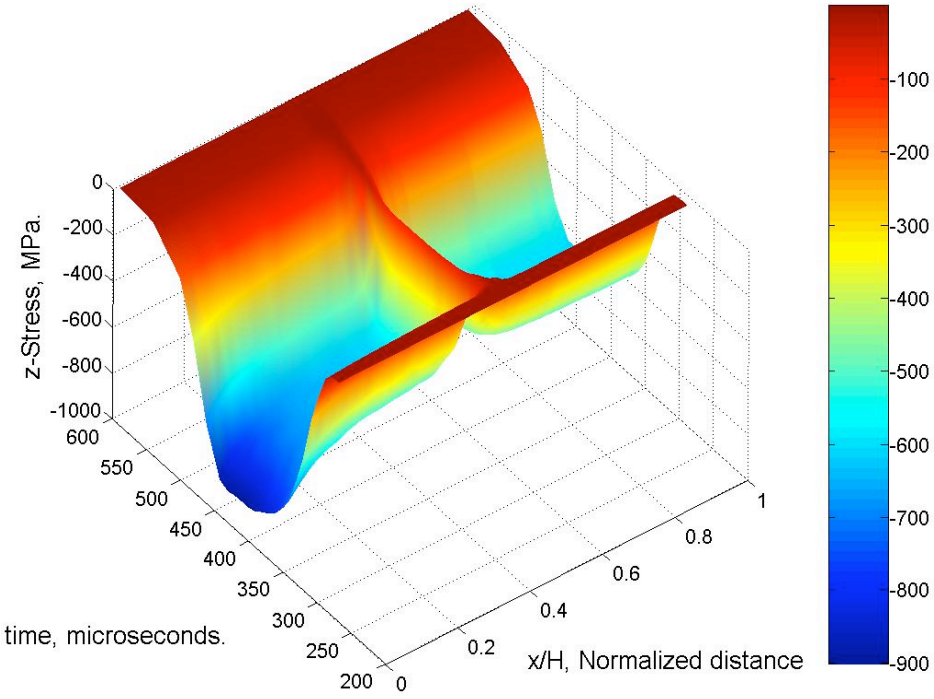

Fig. 17 Z-stress/time/distance map showing response of ceramic/composite sample tested at 20.5 m/s.

Fig. 18 Ceramic/composite sample after testing at 20.5 m/s.

The failure parameters included in the JH-2 model show the general features of damage initiation and propagation as well as the form of stress distribution. The resulting contours of damage are shown in Fig. 18 at two instants during the impact. The damage values are from 0.0 (undamaged) to 1.0 (completely damaged). The ceramic face that was in contact with the incident bar is referred to as

the front surface, and that in contact with the composite, the back surface. Damage first appears on the back face at 340 µsec. Two damage fronts begin to propagate from the back face to the front on the surface of the specimen. At time 364 µsec, one of the damage fronts has already traveled the thickness of the specimen. The first instance of element erosion occurs at time 380 µsec and at 440 µsec, in one of the damage fronts, ceramic material is eroded away along the thickness. The other radial damage front begins to follow a similar trend and axial splitting eventually occurs into at least four major fragments. Material at the back surface is highly damaged. Failure strains were of the order of 0.5 %, corresponding closely to those used by Anderson et al. [23] as well as those measured experimentally.

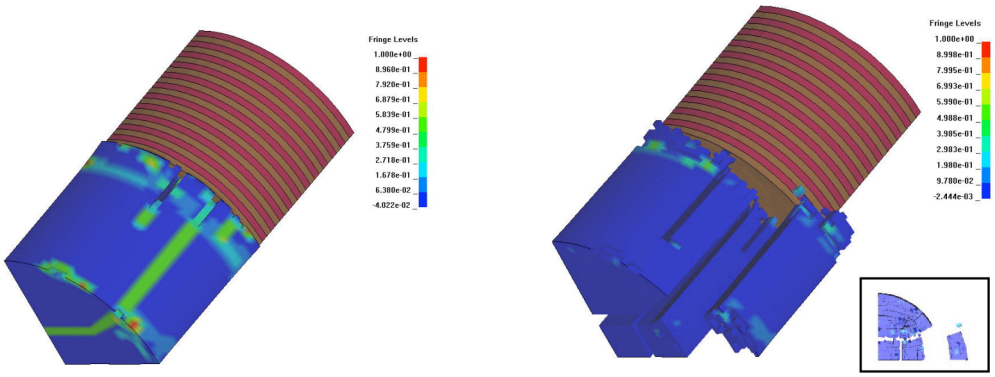

Fig. 19 Contours of damage for ceramic/composite sample at ~ 100µs and ~ 400µs after the beginning of loading, showing development of longitudinal cracking. Inset shows incident bar/ceramic interface.

4.d. 3-layer Ceramic/Rubber/Composite Sample without Interlayer Constraint

Figs. 20 (a) & (b) show experimental and calculated data from the incident and transmitter bars for the unconstrained rubber case tested at 20.5 m/s. For this configuration, the basic shapes and magnitudes of the transmitted waves resemble each other, but it is evident from a change in the experimentally measured reflected wave shape that significant physical damage has begun to occur during the test at a stress of ~ 400MPa.

When unconstrained, the rubber-containing specimens yielded a pseudo-stress/strain curve containing an initial low peak, followed by a low plateau and then a segment which rose rapidly to a stress of 440 MPa at a total of ~8 % strain, Fig. 21.

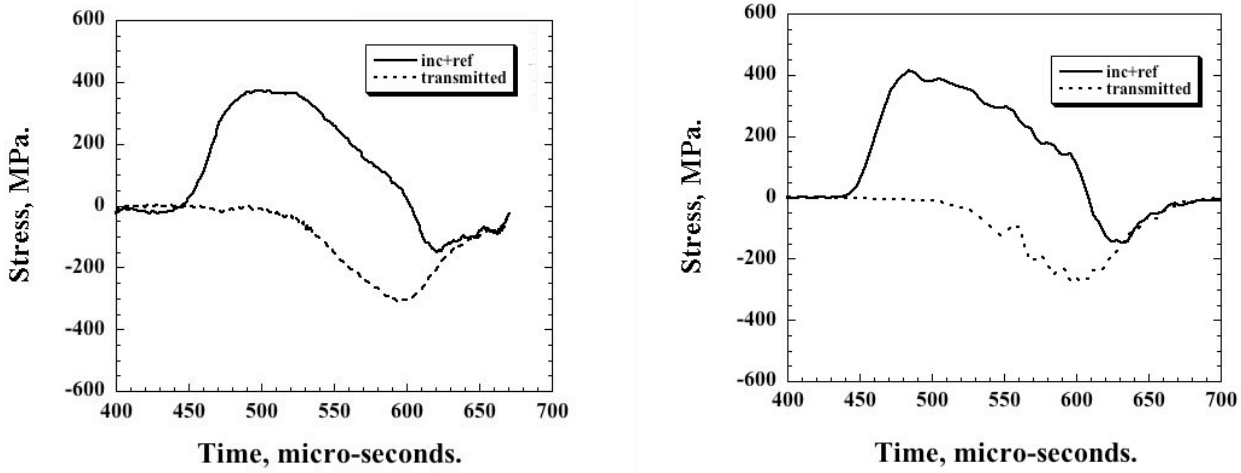

(a) (b)

Fig. 20 Stress on the incident and transmitter bars during a test at 20.5 m/s on an unconstrained ceramic/rubber/composite; a) experimental b) calculated.

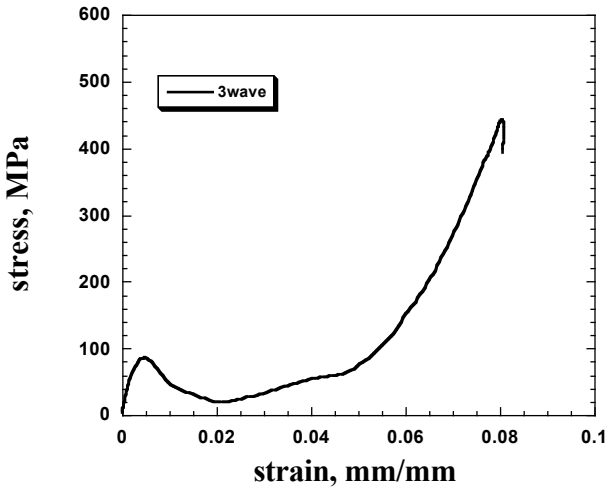

Fig. 21 Pseudo-stress/strain curves for unconstrained ceramic/rubber/composite sample tested at 20.5 m/s.

Fig. 22 shows the evolution with time of the z-stress at the centerline of the unconstrained rubber sample tested at 20.5 m/s as a function of normalized sample length. The modeling clearly shows again that, during high strain rate compression loading of multilayer materials, stress is not distributed uniformly inside the specimen. In particular, severe stress inhomogeneities and discontinuities have been identified in these multi-layer materials and may have serious consequences for the mechanical and other properties.

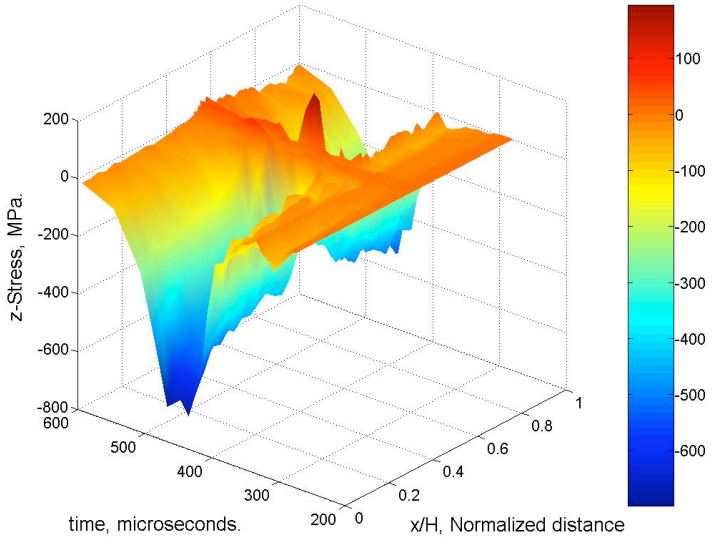

Fig. 22 Z-stress/time/distance map showing response of unconstrained ceramic/rubber/composite sample.

Fig. 23 shows an unconstrained rubber sample after testing in which severe damage has occurred in the ceramic. Lateral expansion of the rubber during the tests gives it a typical plug and annulus appearance after the test.

Fig. 23 Unconstrained ceramic/rubber/composite sample after testing at 20.5 m/s.

Fig. 24 shows the numerical results for damage propagation in the ceramic for the unconstrained rubber sample. For this 3-layer sample, damage initiates at the back surface (at 396 μsec) and the damage front propagates from back to front. Meanwhile damage also initiates at the front face and propagates from front to back. Eventually these two damage fronts meet and axial splitting occurs.

The first signs of damage observed on the surface begin from the front surface and are propagating during the impact event. Heavy crushing can readily be seen at the front and back faces while material erosion is particularly severe at the back face. The ceramic component broke into approximately eight major fragments and several minor ones, numbers that are quite consistent with the evidence of Fig. 23.

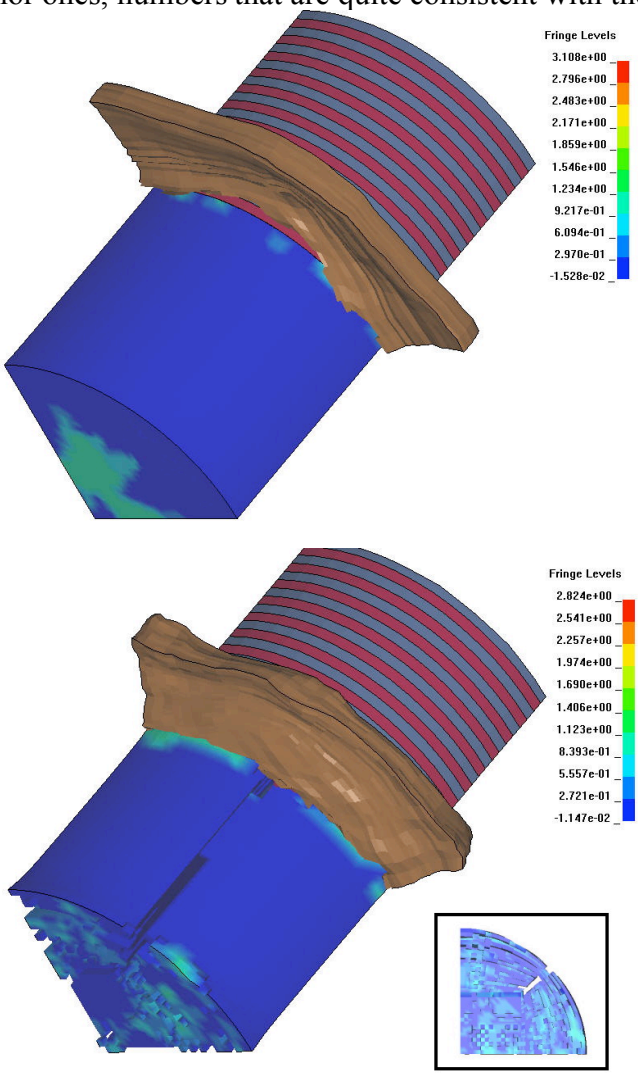

Fig. 24 Contours of damage for unconstrained ceramic/rubber/composite sample ~ 60μs and 200μs after the beginning of loading showing radial expansion and folding of rubber. Inset shows ceramic/incident bar interface.

4.e 3-layer Ceramic/Rubber/Composite Sample with Interlayer Constraint

Figs. 25 (a) & (b) show measured and calculated data from the incident and transmitter bars for the constrained rubber case. The corresponding pseudo-stress strain curve for the constrained rubber sample was steeper and essentially linear right from the start for a total strain of only ~3.8 % at a peak stress of 540 MPa, Fig. 26.

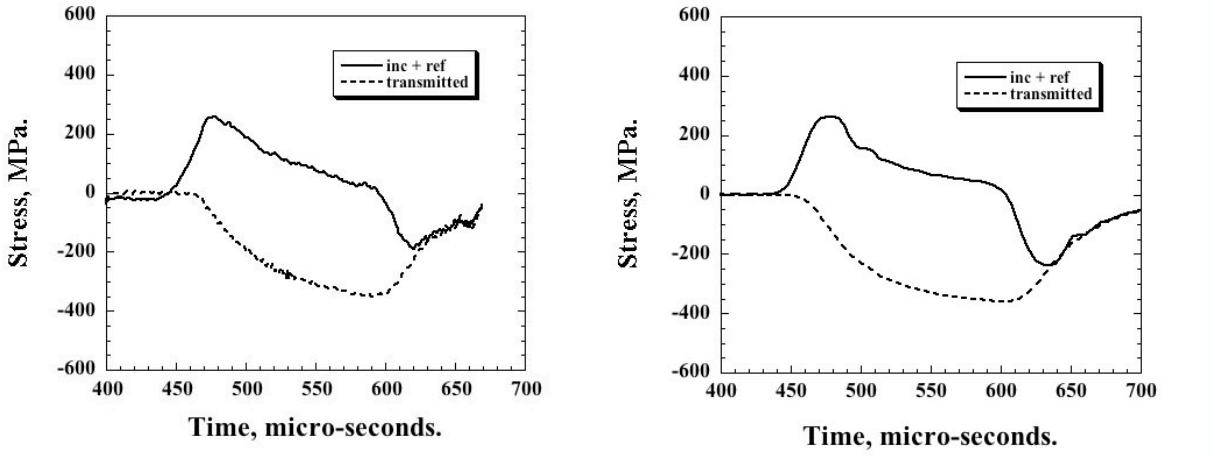

Fig. 25 Stress in the incident and transmitter bars during a test at 20.5 m/s on a ceramic/constrained rubber/composite; a) experimentally measured and, b) calculated.

This strain was barely greater than that experienced by the ceramic/composite sample without any interlayer. Note also that the amplitude of the reflected wave was ~ 390 MPa for the unconstrained rubber case and ~ 260 MPa for the constrained case with corresponding changes in the transmitted wave amplitudes. Fig. 27 shows the evolution with time of the z-stress at the centerline of the constrained rubber sample as a function of normalized sample length. Comparison with Fig. 22 clearly shows the effect of constraint in reducing the stress discontinuity at the interlayer interfaces. Comparison with Fig.17 shows an even more remarkable reduction in stress discontinuity.

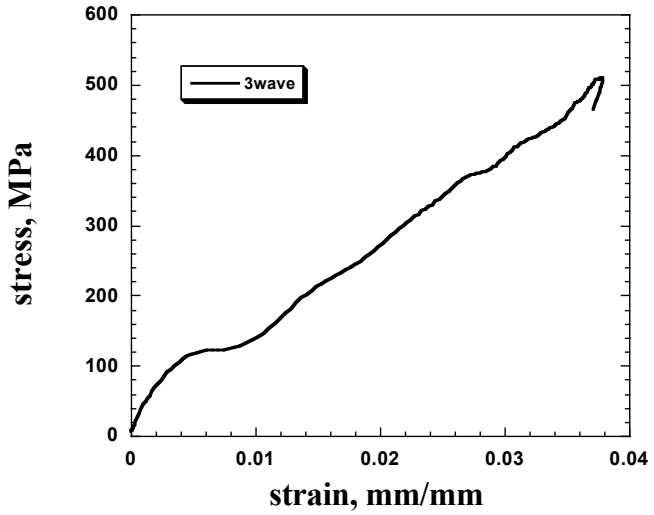

Fig. 26 Pseudo-stress/strain curves for constrained ceramic/rubber/composite sample tested at 20.5 m/s.

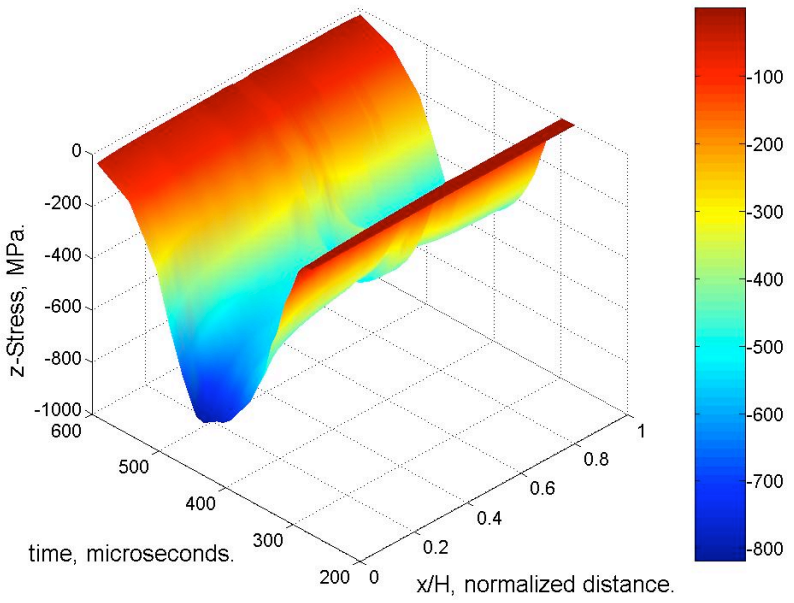

Fig. 27 Z-stress/time/distance map showing response of constrained ceramic/rubber/composite sample.

Fig. 28 shows the calculated damage propagation in the ceramic for the constrained rubber sample. Damage first appears on the front face at 340 μsec. At 364 μsec, three damage fronts begin to propagate from the front face to the back on the surface of the specimen. At the same time, three internal damage fronts are propagating inside the specimen. First element erosion occurs at 368 μsec. At 388 μsec, in one of the damage fronts material is eroded away over almost the half of the thickness value. The other two begin to follow a similar trend. Eventually axial splitting occurs at three different planes and material at the front surface is highly damaged. Constrained rubber significantly decreases the damage content inside the material and also damage is highly localized around the front surface. Ceramic chips also can be seen on the lateral surface of the specimen close to the front surface.

When the rubber interlayer is constrained, its modulus rapidly increases under the compressive stress: the corresponding increase in modulus reduces the acoustic impedance mismatch between ceramic and composite. The result is a relatively smooth transition in z-stress from ceramic to composite, see Fig. 26, without the significant stress discontinuities noted for the other two cases.

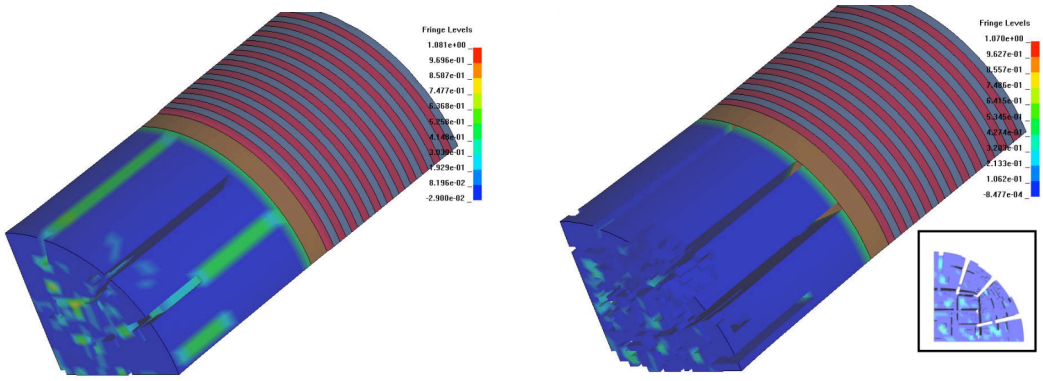

Fig. 28 Contours of damage for constrained ceramic/rubber/composite at ~ 100μs and ~ 400μs after the beginning of loading. Inset shows ceramic/incident bar interface.

High-speed photography revealed that fragment separation usually did not occur during the test but significantly later, typically on impact with the floor afterwards. This was confirmed since a single layer of ordinary adhesive tape wrapped around the ceramic portion of samples before testing which was sufficient to retain the fragments in place. Fig. 29 shows such a tested specimen in which the fragments were retained in place during testing; they have been subsequently highlighted by penetration of blue dye.

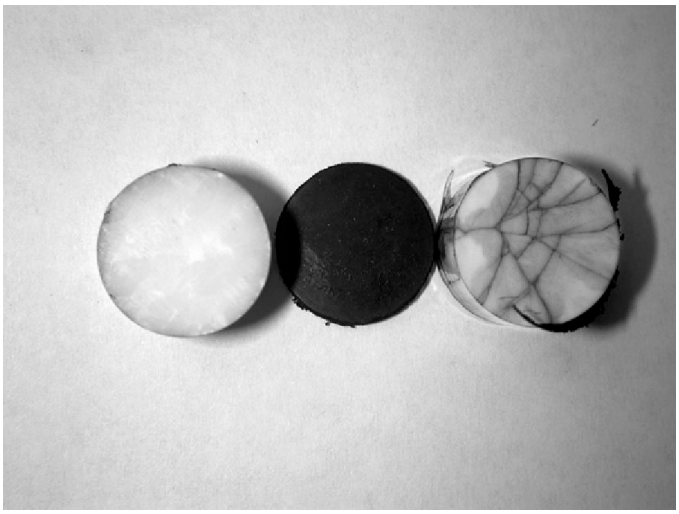

Fig. 29 Constrained ceramic/rubber/composite sample after testing at 20.5 m/s.

It is concluded that the fragments acquire almost no radial momentum during testing and that friction and remaining mechanical interlocking of the fracture surfaces is enough to keep them together. It should be noted, however, that compression of the rubber layer leads to drastically changing reflection and transmission coefficients at the interface and small, transient but non-negligible longitudinal and transverse tensile stresses are commonly observed in the model as a consequence. Note

that plugging of the rubber interlayer does not occur when it is constrained, and the interlayer remains essentially unchanged in appearance, c.f. Fig. 23.

Fig. 30 (a) & (b) shows frames from 2 high-speed photographic sequences taken during a test on an unconstrained rubber sample. The frames of Fig. 30 were taken at about 460 μsec and 480 μsec, at which times the average overall strains were 0.5 % and 1.0 % and, again, no sign of fragment separation is seen. High-speed photography was able to confirm some aspects of the modeling results, however, and Fig. 30(b) shows that the rubber interlayer is squeezed out sideways and folds backwards over the composite in a manner exactly analogous to that predicted by the modeling and illustrated in Fig. 24. Post-test recovery and observation of the ceramic portion of the specimen shown in Fig. 30(a)&(b), confirmed that it had later fragmented completely, even though high-speed photography did not reveal its occurrence.

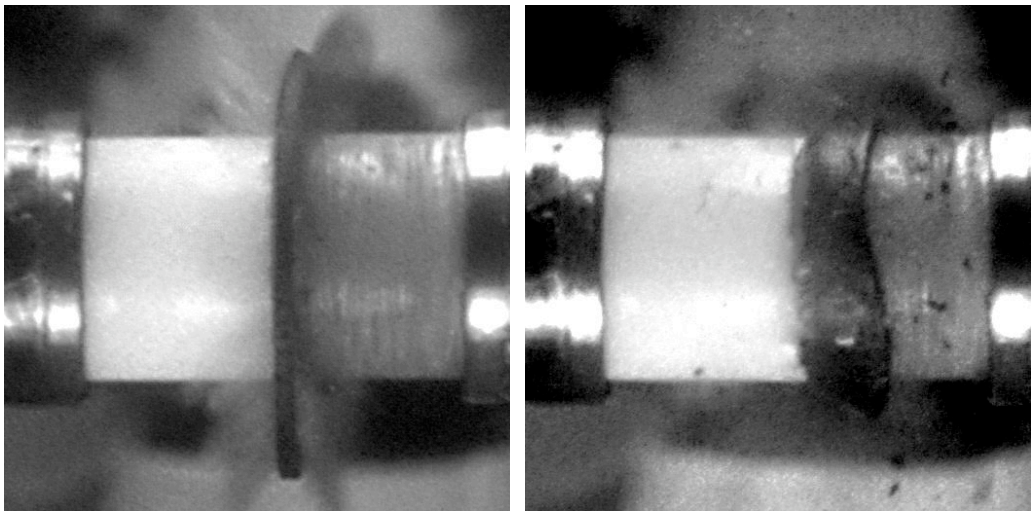

(a) (b)

Fig. 30 High-speed photographs of an unconstrained 3-layer sample at a) ~ 20μs after beginning of loading showing radial expansion of the rubber layer and,
b) ~ 20μs later, showing folding of the rubber over the composite. Compare with Fig. 24.

5. Conclusions

Several prior reports have addressed wave propagation in multi-layer materials similar to the one used here, notably by Fink and Gama *et al*. [24-27]. Following these earlier studies Abrate [28] and Mines [29] recently presented analytical results for the propagation of elastic waves in a lightweight structural armor closely resembling the present material and used Lagrange diagrams to track wave propagation. Abrate [28] showed the presence of tensile spikes in the ceramic and an effective uncoupling of the ceramic from the rubber interlayer. However, all these earlier results were limited to linear elastic responses or did not incorporate damage or only considered 1-dimensional wave propagation.

It is believed that the present results, based on a validated numerical model, mechanical tests and fractographic evidence, present a much more detailed description of the early stages of loading and deformation of multi-layer materials at high strain rates. The following conclusions may be drawn from this work:

1. The SHPB, generally regarded as being only a tool for characterizing homogeneous elastic/plastic materials, can also provide key data for validating numerical models of materials which are non-linear, or of very low or very high impedance relative to the bars, or anisotropic, or composed of several layers of distinctly different materials.
2. Models can provide vastly greater detail concerning the stress/strain/time/location history of the material than experiments alone. The feasibility of accurately modeling stress wave propagation in complex multi-layer materials has thus been demonstrated for the first time.
3. The response of multi-layer materials to the propagation of stress waves is a complex function of many variables and must be addressed through a combination of testing and parallel 3-D modeling rather than either one alone.
4. The introduction of an unconstrained rubber interlayer between the two major structural layers led to a reduction of the maximum stress level in each layer as well as highly inhomogeneous and rapidly varying stress distributions within each layer. The region

close to the unconstrained rubber experienced a reduced stress while the remainder may experience a much higher stress level.

5. Increasing the thickness of the interlayer moves the location of the maximum stress from the striker bar/cer. interface to the cer./Teflon interfaces, indicating that it might also be possible ultimately to control the site of fracture initiation.
6. The effects of confinement of normally low modulus materials can significantly affect their response to wave propagation. (Related research, more fully reported in Ref. [2], shows that expanded Teflon has a distinct advantage over EPDM rubber on account of its low Poisson's ratio. It presents the dual advantages of delaying the passage of the elastic wave into the composite and reducing the amplitude and wavelength of the wave that eventually does pass through. Both of these effects are beneficial in reducing the damage level in the composite backing plate and utilizing the energy absorbing capabilities of the ceramic face plate to the full.)
7. The research has demonstrated the feasibility of extending the current elastic numerical models for high strain rate loading of complex multi-layer materials into the higher strain and strain rate regimes where significant damage begins to occur.
8. The use of mechanical tests along with fractographic and high-speed photographic observations has been demonstrated as a powerful way to validate and refine the modeling effort.

6. Publications

Published/in Press

"Numerical and Experimental Studies of Damage Generation in Multi-Layer Composite Materials at High Strain Rates", A. Tasdemirci and I. W. Hall, Int. Jnl. Impact Eng., in press.

Submitted

"The Effects of Plastic Deformation on Stress Wave Propagation in Multi-Layer Materials" A. Tasdemirci and I. W. Hall.

Presentation

"Experimental and Modeling Studies of Stress Wave Propagation in Multilayer Composite Materials" I. W. Hall & A. Tasdemirci, Army Research Laboratory, Aberdeen, MD, 1/4/06.

Bibliography

1. **Tasdemirci, A., et al., *Stress wave propagation effects in two- and three-layered composite materials.* Journal Of Composite Materials, 2004. 38(12): p. 995-1009.**
2. **Tasdemirci, A. and I.W. Hall, *Experimental and modeling studies of stress wave propagation in multilayer composite materials: Low modulus interlayer effects.* Journal Of Composite Materials, 2005. 39(11): p. 981-1005.**
3. **Guden, M. and I.W. Hall, *Dynamic properties of metal matrix composites: a comparative study.* Materials Science and Engineering a-Structural Materials Properties Microstructure and Processing, 1998. 242(1-2): p. 141-152.**
4. **Holmquist, T.J. and G.R. Johnson, *Response of silicon carbide to high velocity impact.* Journal of Applied Physics, 2002. 91(9): p. 5858-5866.**
5. **Holmquist, T.J. and G.R. Johnson, *Modeling projectile impact onto prestressed ceramic targets.* Journal De Physique Iv, 2003. 110: p. 597-602.**
6. **Holmquist, T.J., D.W. Templeton, and K.D. Bishnoi, *High strain rate constitutive modeling of aluminum nitride including a first-order phase transformation.* Journal De Physique Iv, 2000. 10(P9): p. 21-26.**
7. **Holmquist, T.J., D.W. Templeton, and K.D. Bishnoi, *Constitutive modeling of aluminum nitride for large strain, high-strain rate, and high-pressure applications.* International Journal of Impact Engineering, 2001. 25(3): p. 211-231.**
8. **Johnson, G.R. and T.J. Holmquist, *Response of boron carbide subjected to large strains, high strain rates, and high pressures.* Journal of Applied Physics, 1999. 85(12): p. 8060-8073.**
9. **Johnson, G.R., T.J. Holmquist, and S.R. Beissel, *Response of aluminum nitride (including a phase change) to large strains, high strain rates, and high pressures.* Journal of Applied Physics, 2003. 94(3): p. 1639-1646.**
10. **Johnson, G.R., et al., *An algorithm to automatically convert distorted finite elements into meshless particles during dynamic deformation.* International Journal of Impact Engineering, 2002. 27(10): p. 997-1013.**
11. **Chen, W., *Dynamic Failure Behavior of Ceramics Under Multiaxial Compression*, in *Mechanical Engineering*. 1995, California Institute of Technology: Pasedana, California. p. 208.**
12. **Chen, W. and G. Ravichandran, *Failure mode transition in ceramics under dynamic multiaxial compression.* International Journal of Fracture, 2000. 101(1-2): p. 141-159.**
13. **Gama, B.A., G. Ma, J. W. Gillespie, Jr., and B. Cheeseman. *A Modified JH-2 Model with Tension Cut-off Criteria in Simulating Sherman's Experiment on Confined Ceramics*. in *Advanced Computing and Simulation, 23rd Army Science Conference*. 2002. Orlando, FL.**
14. **Anderson, C.E., G. Johnson, and H. T. *Ballistic Experiments and Computations of Confined 99.5% Al_2O_3 Ceramic Tiles*. in *15th International Symposium on Ballistics*. 1995.**
15. **Abrate, S., *Modeling of Impact on Composite Structures.* Comp. Struct., 2001. 51: p. 129-138.**
16. **Richardson, M.O.W. and M.J. Wisheart, *Review of low-velocity impact properties of composite materials.* Composites Part a-Applied Science and Manufacturing, 1996. 27(12): p. 1123-1131.**
17. **Choi, H.Y. and F.K. Chang, *A Model for Predicting Damage in Graphite Epoxy Laminated Composites Resulting from Low-Velocity Point Impact.* Journal of Composite Materials, 1992. 26(14): p. 2134-2169.**
18. **Davies, G.A.O. and X. Zhang, *Impact Damage Prediction in Carbon Composite Structures.* International Journal of Impact Engineering, 1995. 16(1): p. 149-170.**

19. **Yen, C.F.** ***Ballistic impact modeling of composite materials.*** **in** ***7th International LS-DYNA Users Conference.*** **2002. Dearborn, Michigan: Livermore Software Technology Corporation (LSTC) and Engineering Technology Associates, Inc. (ETA).**
20. **Tasdemirci, A. and I.W. Hall,** ***Numerical and Experimental Studies of Damage Generation in Multi-Layer Composite Materials at High Strain Rates.*** **International Journal of impact Engineering, accepted for publication, 2005.**
21. **Grady, D.E.,** ***Shock-wave compression of brittle solids.*** **Mechanics of Materials, 1998. 29(3-4): p. 181-203.**
22. **Ashby, M.F. and C.G. Sammis,** ***The Damage Mechanics Of Brittle Solids In Compression.*** **Pure And Applied Geophysics, 1990. 133(3): p. 489-521.**
23. **Anderson, C.E., et al.,** ***Numerical Simulations of Shpb Experiments for the Dynamic Compressive Strength and Failure of Ceramics.*** **International Journal of Fracture, 1992. 55(3): p. 193-208.**
24. **Fink, B.K.,** ***Performance metrics for composite integral armor.*** **Journal of Thermoplastic Composite Materials, 2000. 13(5): p. 417-431.**
25. **Gama, B.A., Gillespie, J. W. Jr., Mahfuz, H., Bogetti, T.A. and Fink, B.,.** ***Effect of Non-Linear Material Behavior on the Through-Thickness Stress Wave Propagation in Multi-Layer Hybrid Lightweight Armor.*** **in** ***Advances in Comp. Eng. and Sci.*** **2000: Tech. Sci. Press.**
26. **Gama, B.A., Gillespie, J. W. Jr., Bogetti, T. A. and Fink, B.,.** ***Innovative design and ballistic performance of Lightweight Composite Integral Armor.*** **in** ***SAE 2001 World Congress.*** **2001. Detroit, MI: SAE.**
27. **Gama, B.A., et al.,** ***Aluminum foam integral armor: a new dimension in armor design.*** **Composite Structures, 2001. 52(3-4): p. 381-395.**
28. **Abrate, S.,** ***Wave propagation in lightweight composite armor.*** **Journal De Physique Iv, 2003. 110: p. 657-662.**
29. **Mines, R.A.W.,** ***A one-dimensional stress wave analysis of a lightweight composite armour.*** **Composite Structures, 2004. 64(1): p. 55-62.**